W. Lipiński[1]
e-mail: lipinski@umn.edu

J. H. Davidson

Department of Mechanical Engineering,
University of Minnesota,
Minneapolis, MN 55455

S. Haussener
Institute of Mechanical Engineering,
EPFL
Lausanne 1015, Switzerland;
Environmental Energy Technologies Division,
Lawrence Berkeley National Laboratory,
Berkeley, CA 94720

J. F. Klausner

A. M. Mehdizadeh

Department of Mechanical and
Aerospace Engineering,
University of Florida,
Gainesville, FL 32611

J. Petrasch
Energy Research Center,
Vorarlberg University of Applied Sciences,
Dornbirn 6850, Austria

A. Steinfeld
Department of Mechanical and
Process Engineering,
ETH Zurich,
Zurich 8092, Switzerland;
Solar Technology Laboratory,
Paul Scherrer Institute,
Villigen 5232, Switzerland

L. Venstrom
Department of Mechanical Engineering,
University of Minnesota,
Minneapolis, MN 55455

Review of Heat Transfer Research for Solar Thermochemical Applications

This article reviews the progress, challenges and opportunities in heat transfer research as applied to high-temperature thermochemical systems that use high-flux solar irradiation as the source of process heat. Selected pertinent areas such as radiative spectroscopy and tomography-based heat and mass characterization of heterogeneous media, kinetics of high-temperature heterogeneous reactions, heat and mass transfer modeling of solar thermochemical systems, and thermal measurements in high-temperature systems are presented, with brief discussions of their methods and example results from selected applications. [DOI: 10.1115/1.4024088]

Keywords: heat transfer, solar thermochemistry, solar reactor, reacting media, modeling, experimental

1 Introduction

Heat transfer in chemically reacting media is a complex transient phenomenon typically encountered in combustion, fuels and materials processing, extractive metallurgy, and other high-temperature processes involving media of time-dependent composition and thermophysical properties. Of special interest are endothermic processes that make use of concentrated solar radiation as the source of process heat [1–3]. Solar thermochemical processes are suitable for production of fuels, in which solar energy is stored in form of chemical bonds, and chemical commodities for industrial, agricultural, and other applications. Examples of solar thermochemical processes for fuel production include upgrading fossil fuels [4–6] and biomass [7], thermal reduction of metal oxides [8–12], and direct water thermolysis [13]. While the majority of processes considered in the past were for production of hydrogen, production of both hydrogen and carbon monoxide—the components of the synthesis gas, which can be further processed to hydrocarbon fuels—is of current research focus. Examples of solar thermochemical processes for production of chemical commodities are the thermal decomposition of limestone [14] and ammonia [15]. Solar process heat is also suitable for recycling of hazardous waste materials [16] and CO_2 capture [17].

High-temperature solar chemical reactors are designed for maximum solar-to-chemical energy conversion efficiency to minimize the required size of the optical concentrators and, thus, improve the economic viability [18]. In a solar thermochemical reactor, the incident solar radiation enters a cavity through an aperture, which in turn may be windowed. A portion of the incident radiation is absorbed by the cavity walls and reactants, and a portion is lost through the aperture. The reactors typically feature heterogeneous reacting media in form of macrostructures, microstructures, or particulate media such as packed beds, fluidized beds, and suspensions at temperatures exceeding 1000 K, and in some applications

[1]Corresponding author.

Manuscript received October 13, 2012; final manuscript received March 9, 2013; published online May 17, 2013. Assoc. Editor: S. A. Sherif.

reaching more than 2000 K. Such media serve a multipurpose role. They absorb high-flux irradiation (absorption is predominantly by the solid phase as the direct gas absorption is ineffective for length-scales of a solar reactor) and transfer the heat to the chemical reaction. In directly irradiated reactors, the incident radiation or its portion is absorbed by a solid that is involved in the chemical reaction, e.g., Refs. [19–22]. In indirectly irradiated reactors, the incident radiation is absorbed by a chemically inert solid and then transferred to the chemical reaction by conduction, convection, and radiation through an intermediate heat transfer medium (solid, fluid, or multiphase), e.g., Refs. [6,14,23].

Thermal transport processes are an area where physics has extensively been studied at discrete spatial levels varying from nanoscale to microscale to macroscale [24–27]. However, accurate characterization and comprehensive simulation techniques connecting discrete and continuum levels, in particular for chemically reacting media, still need to be developed for effective analyses of complete reactors. Such techniques are highly desired for direct design and optimization of reactors featuring prescribed materials of unknown continuum characteristics. Advancements in materials and computational sciences have enabled, however, an even more intriguing but less explored approach of materials-by-design, in which materials of prescribed continuum characteristics indicated by predictive reactor-level models are inversely engineered by targeted identification of suitable composition and morphology [28–30]. Both direct thermal characterization and materials-by-design approaches are useful for understanding and optimizing the complex thermal transport processes and, consequently, for achieving the ultimate high efficiencies of solar reactors. The desired characteristics of an absorbing and reacting material must allow for (i) efficient absorption of incident concentrated solar radiation, (ii) rapid heat transfer between the absorption and reaction sites, (iii) confinement of the emitted thermal radiation in the close vicinity of the reaction site, and (iv) minimum heat losses from the reacting medium by conduction and convection. While a particular material design satisfying these conditions strongly depends on a specific application, any design and optimization efforts for high-temperature solar thermochemical applications can be summarized as minimization of irreversibilities associated with heat and reactant transport to the reaction site and transport of products from the reaction site.

The idea of using concentrated solar radiation for driving chemical reactions is not new—it dates back to at least the 18th century, when Antoine Lavoisier conducted combustion experiments in his solar furnace consisting of two concentric lenses [31], and significant pioneering work on solar processes and reactors was already done several decades ago, among others by Trombe and Foex [32], Nakamura [33], and Fletcher and Moen [34]. The progress in solar thermochemistry, an emerging field of science and technology, towards efficient and economically viable technical implementation necessitates addressing fundamental challenges associated with effective heat and mass transfer, rapid chemical kinetics and enhanced material durability, as well as developing reliable measurement, diagnostics, and control techniques due to extreme conditions imposed by high heat fluxes and temperatures, and the inherently transient nature of solar irradiation.

This article summarizes the state-of-the-art research in the field of heat transfer as applied to solar thermochemical systems. Radiative spectroscopy and tomography-based heat and mass characterization of heterogeneous media, kinetics of high-temperature heterogeneous reactions, heat and mass transfer modeling of solar thermochemical systems, and thermal measurements in high-temperature systems are discussed for selected solar thermochemical processes.

2 Radiative Spectroscopy Characterization of Solar Reacting Media

In high-temperature solar thermochemical applications the contribution of thermal radiation to the energy equation is of primary interest. Modeling radiative heat transfer involves determination of the spectral radiative intensity I_λ traveling through an absorbing, emitting, and scattering medium by solving the equation of radiative transfer. For a medium at temperature T for which the time scale associated with variations of temperature and physical properties is much larger than that associated with radiation propagation, the quasi-steady equation of radiative transfer is formulated as [35]

$$\frac{\mathrm{d}I_\lambda(\vec{\mathbf{r}},\hat{\mathbf{s}})}{\mathrm{d}s}+\beta_\lambda I_\lambda(\vec{\mathbf{r}},\hat{\mathbf{s}})=\kappa_\lambda I_{\lambda,\mathrm{b}}(\vec{\mathbf{r}})+\frac{\sigma_{\mathrm{s},\lambda}}{4\pi}\int_{\Omega_{\mathrm{in}}=0}^{4\pi} I_\lambda(\vec{\mathbf{r}},\hat{\mathbf{s}}_{\mathrm{in}})\Phi_\lambda(\vec{\mathbf{r}},\hat{\mathbf{s}},\hat{\mathbf{s}}_{\mathrm{in}})\mathrm{d}\Omega_{\mathrm{in}} \tag{1}$$

where I_λ is the spectral radiative intensity, κ_λ, $\sigma_{\mathrm{s},\lambda}$ and β_λ are the spectral absorption, scattering and extinction coefficients, respectively, and Φ_λ is the spectral scattering phase function. Integration of Eq. (1) over the solid angle 4π and the entire wavelength spectrum results in the total divergence of the radiative flux

$$\nabla\cdot\vec{\mathbf{q}}''(\vec{\mathbf{r}})=\int_0^\infty \kappa_\lambda\left[4\pi I_{\mathrm{b},\lambda}(\vec{\mathbf{r}})-G_\lambda(\vec{\mathbf{r}})\right]\mathrm{d}\lambda,\qquad G_\lambda(\vec{\mathbf{r}})=\int_{\mathrm{d}\Omega_{\mathrm{in}}=0}^{4\pi} I_\lambda(\vec{\mathbf{r}},\hat{\mathbf{s}})\mathrm{d}\Omega_{\mathrm{in}} \tag{2}$$

where G_λ is the spectral incident radiation. Equation (1) is valid for media that can be represented as a single radiatively participating continuum, characterized by single temperature and radiative intensity. However, in many instances multicomponent approaches need to be employed at the continuum level to correctly account for the heterogeneous nature of the medium. An example is a packed bed of large semitransparent limestone particles used for solar thermochemical production of lime [36]. Some aspects of multicomponent continuum radiative transfer modeling are discussed in Refs. [37,38] and literature cited therein.

Accurate analysis of radiative heat transfer, guiding the engineering design and optimization for maximum solar energy conversion efficiency, requires a detailed knowledge of optical and radiative properties as a function of temperature, wavelength, direction, and composition in the relevant spectral range, which includes visible (VIS) and near-infrared (NIR) radiation. The properties are typically predicted by using theoretical models for systems with defined morphology, and determined by combined numerical–experimental studies for complex media containing structures in a broad size [39]. In the latter approach, the measured transmitted and reflected radiative fluxes are the input to either direct iterative or inverse numerical models that, in turn, are used to infer the radiative properties of interest such as the spectral extinction coefficient β_λ, the spectral scattering albedo ω_λ, and the spectral scattering phase function Φ_λ. The presence of a chemical reaction additionally complicates the experimental procedures and in situ measurements of radiative characteristics due to changing composition and, thus, property variations.

Experimental setups for studying radiative heat transfer in participating media typically involve a sample medium irradiated by a collimated beam of radiation. The radiation exiting the sample can then be measured by a number of different methods. In the simplest approach a fraction of the transmitted radiation is measured by a detector placed directly at the sample's boundary, opposite to the irradiated side. One or two integrating spheres are usually incorporated for directional-hemispherical transmittance and reflectance experiments in which the overall transmitted and reflected fluxes are of interest, for example, when aiming at determining transport approximation based radiative properties. As the angular distribution of transmitted and reflected fluxes can be highly nonuniform for heterogeneous media, complex goniometry systems capable of measuring the transmitted and reflected fluxes within a narrow solid angle around the viewing direction are usually employed. A summary of the aforementioned methods can be found in the textbook by Modest [35] and the review papers by

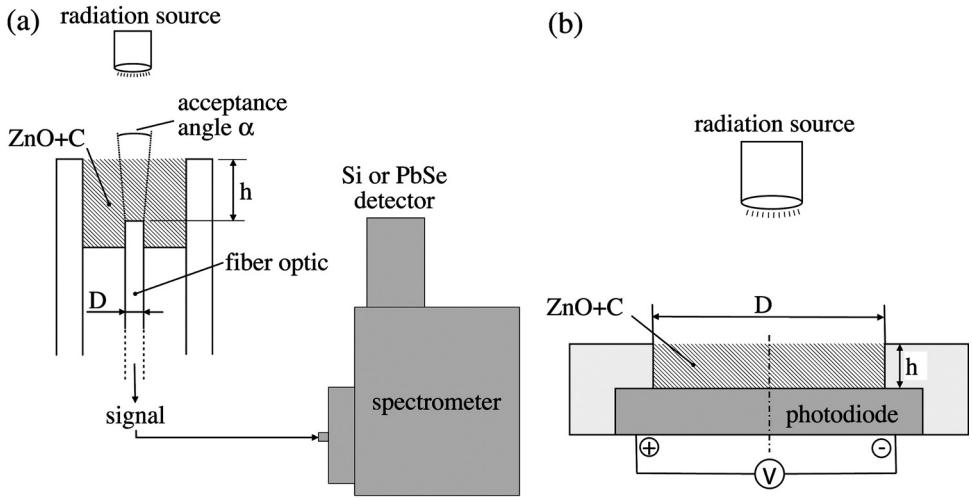

Fig. 1 Experimental setups for radiative measurements with packed beds of ZnO and beech charcoal [42]: (*a*) a fiber optics coupled to a spectrometer, and (*b*) a photodiode detector. (Reproduced with permission from Taylor & Francis.)

Baillis and Sacadura [39] and Agarwal and Mengüç [40]. Selected combined experimental–numerical studies of radiative properties of participating media encountered in solar thermochemical applications are briefly outlined in the following text.

The thermal production of Zn by carbothermic reduction of ZnO was demonstrated using a packed-bed solar reactor containing a mixture of ZnO and beach charcoal undergoing shrinking due to the carbothermic reduction [41]. The extinction coefficient of the mixture was determined in Ref. [42] at ambient temperature using two experimental setups shown in Fig. 1. In the first setup, shown in Fig. 1(*a*), radiation in the range 500–1000 nm was captured by a 200 μm-diameter fiber optics and sent to a spectrometer equipped with a Si/PbSe detector. In the second setup, radiation in the range 350–1100 nm was captured by a 5 mm-diameter Si photodiode. Both setups measured attenuation of radiation from a 3273 K blackbody source. The Monte Carlo ray-tracing method was employed to infer the extinction coefficient from the measured radiative fluxes. The extinction coefficient was determined to be $10{,}103 \pm 615\,\mathrm{m}^{-1}$ at 1000 nm using the setup of Fig. 1(*a*) and $7850 \pm 337\,\mathrm{m}^{-1}$ for the range 350–1100 nm using the setup of Fig. 1(*b*), revealing a very short mean free path of radiation propagation for the considered material. To reduce the optical thickness of the highly attenuating ZnO and C powder beds, large ($>100\,\mu$m) semitransparent SiO_2 particles were proposed in Ref. [43] as an addition to the ZnO and C particulates. The monochromatic transmittance of packed-bed mixtures of SiO_2, ZnO, and C particles of various relative mass fractions was measured at 632.8 nm as a function of the packed-bed thickness using a He-Ne laser/fiber optics/spectrometer system. The measured transmittance was used to validate a Monte Carlo model for a pseudocontinuum multicomponent medium containing polydispersed Mie-scattering particles [44]. The model was in turn used to determine the radiative properties such as the extinction coefficient, the scattering albedo, and the scattering phase function of the packed-bed mixtures.

A spectroscopic goniometry system for measurements of directional and spectral characteristics of highly attenuating semitransparent media typical for solar thermal and thermochemical applications is presented in Ref. [45]. The system, shown in Fig. 2, incorporates a double monochromator coupled to a double radiation source and a rotary multielement sandwich detector to enable measurements in the spectral range between 0.3–4 μm. Direct iterative and inverse radiative transfer techniques are employed to extract radiative properties of interest from bidirectional reflectance and transmittance measurements. The setup presented in Ref. [45] is primarily designed for bidirectional transmittance and reflectance measurements, in particular normal–directional transmittance [46], and further allowing for normal–"wide-angle" (detector on sample) transmittance [47] measurements after minor modifications of the optical configuration. Two examples demonstrating the feasibility of the method are given in Ref. [45], the determination of the extinction coefficient of reticulate porous ceramics (RPC) with a nominal pore size of 2.54 mm and porosity of 0.91, and the extraction of a complete set of radiative properties for a packed bed of μm-sized particles ZnO particles of approximately 0.40–0.45 porosity. The experimental results obtained with RPC and shown in Fig. 3 were found to be in good agreement with a pore-level Monte Carlo simulation on a tomography scan of the RPC sample, with the log-linear slope of the exponential fit to the data resulting in an apparent extinction coefficient of $\beta = (230 \pm 20)\ \mathrm{m}^{-1}$ and the Monte Carlo solution giving $\beta = (210 \pm 20)\ \mathrm{m}^{-1}$ [45,46]. For the ZnO packed bed, a Monte Carlo ray-tracing simulation of the setup was used to infer the radiative properties from the experimental results [45,47]. The radiative properties inferred iteratively were the extinction coefficient $\beta = 35{,}000\,\mathrm{m}^{-1}$, the scattering albedo $\omega = 0.999$, and a scattering phase function based on a double Dirac δ approximation. Unlike the analogous Fig. 3, a log-linear fit to the data-points shown in Fig. 4 does not intersect the vertical axis at 1 but at much lower values. The simulation results shown in Fig. 4 indicate that in the limit of very thin samples a log-linear fit would have a much

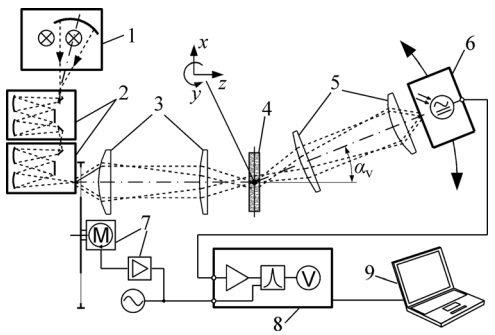

Fig. 2 Spectroscopic goniometry system for measurements of directional and spectral characteristics of highly attenuating semitransparent media [45]: (1) dual Xe-arc/Cesiwid globar lamp, (2) double monochromator, (3) and (5) imaging lens pairs, (4) sample, (6) rotary detector, (7) beam chopper, (8) lock-in amplifier, and (9) data acquisition system. The *x-y-z* coordinate system is centered at the pivot point. (Reproduced with permission from Taylor & Francis.)

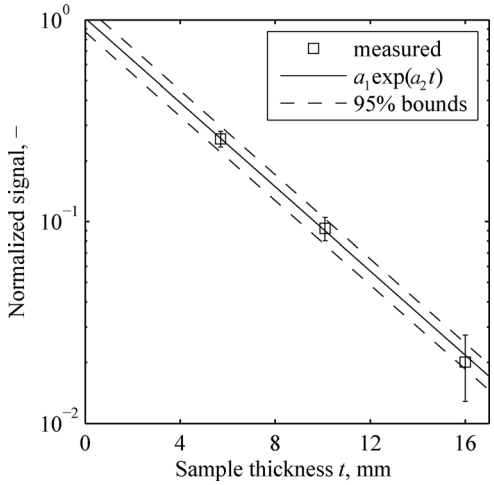

Fig. 3 Normalized detector signal in forward direction plotted against three different RPC sample thicknesses at a wavelength of 500 nm and an acceptance opening half angle of 3.6 deg [45,46]. The solid line shows the best fit of the exponential function $S = a_1 \exp(a_2 t)$, with S denoting the normalized signal and t the sample thickness. The 95% uncertainty limits are illustrated by the error bars and the dashed lines. (Reproduced with permission from Taylor & Francis.)

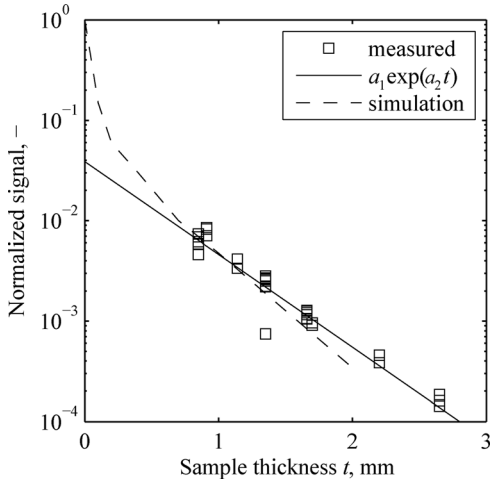

Fig. 4 Normalized detector signal in forward direction for different thicknesses of a ZnO packed-bed sample at a wavelength of 1000 nm [45,47]. The measurement was performed by placing a detector directly on the sample surface, which is equivalent to integrating over an angular range of ±60 deg. The exponential fit is the same type as shown in Fig. 3, but this time it has a significant vertical-axis offset with respect to 10^0.

steeper slope. The subsequent decrease in slope is caused by inscattered radiative power, which increases with the number of scattering events and, consequently, sample thickness until a plateau (the diffusion limit) is reached.

Porous cerium dioxide (ceria) ceramics were recently proposed as a novel reactive material to realize solar-driven thermochemical cycles to split water and carbon dioxide for production of synthesis gas [10,22]. Ceria ceramics are weakly absorbing in wavelength range 0.5–2 μm and highly scattering in the near-infrared [48,49]. As a result, directional-hemispherical transmittance of ceria ceramics is low, on the order of 1% for samples of about 1-mm geometrical thickness, due to very large optical thickness. A combined experimental–numerical methodology to identify visible and near-infrared properties of ceria ceramics over the wavelength range 0.35–2 μm was developed in Refs. [50,51] to overcome difficulties of the identification procedure for optically thick media that are highly scattering over a large portion of the spectrum. The methodology also circumvents the challenges in the identification procedure due to unknown index of absorption of ceria in the spectral range of weak absorption. Directional–hemispherical reflectance was used to retrieve transport scattering albedo by employing the analytical solution based on the modified two-flux method. The experimental setup used to measure directional–hemispherical reflectance in the spectral range 0.35–2 μm consisted of a PerkinElmer Lambda 1050 spectrophotometer equipped with source lamps, double monochromators optical filters, and a chopper contained in the source compartment, with the sample holder mounted to the reflectance port of the integrating sphere. Complementary binormal narrow-cone transmittance measurements were performed in the spectral range 0.9–1.7 μm by a more sophisticated setup capable of resolving binormal transmittance of 0.001% was employed. A 300 W short arc Xe lamp was used along with a Newport MS 257 monochromator as the source of monochromatic radiation. The binormal narrow-cone transmittance was used to determine the transport extinction coefficient in a narrow spectral range 0.9–1.4 μm by iterative Monte Carlo ray-tracing technique. Mie scattering theory was applied to polydisperse pores and grains to extend the spectral range of identification. Transport radiative properties were determined for types of ceria samples, with porosity of 0.08 and 0.72, respectively. The transport scattering albedo extracted from the directional–hemispherical reflectance was found to be close to unity for both sample types. The transport scattering coefficient computed by Mie theory was found to weakly decrease for the dense ceramics with increasing wavelength in the range of weak absorption. The latter effect was explained by monotonically increasing scattering efficiency factor with the diffraction parameter of large single pores for low relative refractive index $1/n$. In addition, the absorption index of bulk ceria was determined.

3 Tomography-Based Characterization of Solar Reacting Media

Computed tomography (CT) enables digital geometrical representation of complex heterogeneous media, which in turn is used for the direct pore-level numerical simulations (DPLS). Morphological characteristics, radiative properties, thermal conductivity, interfacial heat transfer coefficient, permeability, Dupuit–Forchheimer coefficient, tortuosity and residence time distributions, and dispersion tensor can directly be computed using the exact geometry of the media. A detailed discussion of the comprehensive CT-based morphological and thermal transport characterization methodology for heterogeneous media can be found in Refs. [36–38,52–59], and is omitted from this article for brevity. CT-based DPLS was applied, among others, to determine the effective transport properties of a Rh-coated SiC RPC used for the solar reforming of CH_4 [56–59], of a packed bed of semitransparent $CaCO_3$ particles used for the solar production of lime and cement [36], of an RPC used for the solar thermal dissociation of H_2SO_4 [60], of a reacting packed bed of carbonaceous materials undergoing gasification [61,62], and of an anisotropic ceria monolith used for the splitting of H_2O and CO_2 via redox cycles [63].

As an example of application of the CT-based DPLS, heat and mass transfer characteristics of an RPC with 20 ppi and $d_{nom} = 1.27$ mm investigated in Ref. [60] are presented here. The RPC sample is shown in Fig. 5. Low-resolution CT was applied by exposing the sample to an unfiltered polychromatic X-ray beam for voxel sizes of typically 15 μm. 3D surface rendering of a sample subvolume, reconstructed from the resulting tomography data, is depicted in Fig. 5(*b*). Figure 5(*c*) shows a 2D image of a single RPC strut obtained by high-resolution CT of 0.37 μm voxel size with the synchrotron light source (SLS) of the Paul Scherrer Institute. The calculated specific surface area was 1680 m^{-1}. The calculated cumulative radiative extinction distribution function obtained for this material is shown in Fig. 6(*a*), leading to the extinction coefficient of 431 m^{-1}. Additionally, data points measured by one

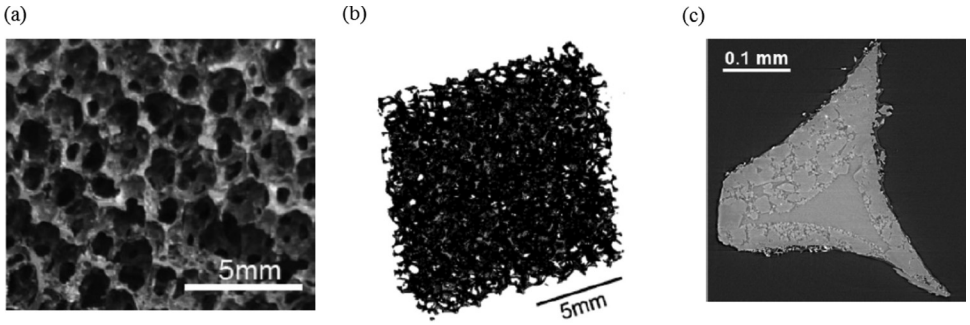

Fig. 5 Sample of RPC foam: (*a*) top-view photograph and (*b*) 3D surface rendering of a 15 μm voxel size tomogram; (*c*) 2D image of a single strut obtained by high-resolution CT of 0.37 μm voxel size [60]

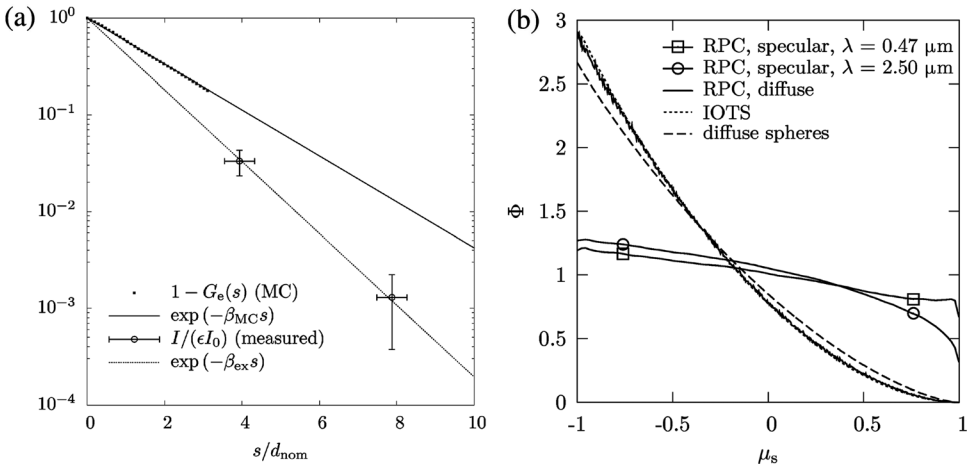

Fig. 6 Tomography-based Monte Carlo ray-tracing radiative characterization of an RPC: (*a*) calculated cumulative distribution of extinction path length versus experimentally measured radiation intensity as a function of sample thickness, and (*b*) scattering phase functions calculated assuming diffusely or specularly reflecting strut surfaces [60]

of the previously introduced spectroscopy setups are indicated, allowing for an experimental estimation of the extinction coefficient of 628 m^{-1}. The scattering phase function (depicted as a function of the cosine of the scattering angle, μ_{s}) is shown in Fig. 6(*b*) and it was computed assuming either diffusely or specularly reflecting strut surfaces. For comparison, the scattering phase functions of a bed of identical overlapping transparent spheres (IOTS) and a diffuse sphere are also shown in Fig. 6(*b*). The scattering phase function for diffusely reflecting surfaces was found to be almost independent of the medium morphology. Solving the energy, mass, and momentum conservation equations in the fluid phase of the RPC resulted in the velocity, temperature, and pressure fields. The pressure drop through the RPC led to a permeability of 5.7×10^{-8} m^2 and a Dupuit–Forchheimer coefficient of 519 m^{-1}. The solid–fluid interface heat transfer was found to be well described by the relation $\mathrm{Nu} = 6.82 + 0.20\ \mathrm{Re}^{0.79}\ \mathrm{Pr}^{0.61}$, and is graphically presented in Fig. 7. The calculated tortuosity distribution through the sample, shown in Fig. 8, resulted in a mean tortuosity of 1.07.

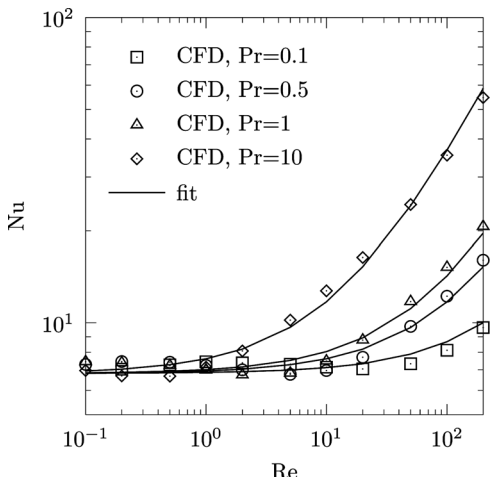

Fig. 7 Nu number as a function of Re and Pr numbers [60]

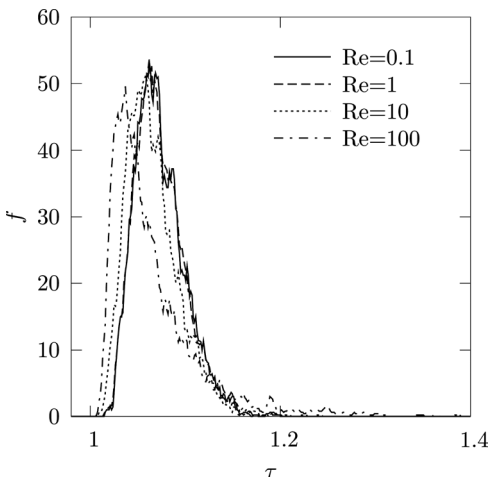

Fig. 8 Tortuosity distribution as a function of Re number [60]

4 Kinetics of High-Temperature Solar Reactions

The knowledge of chemical reaction rates is needed for conjugate heat and mass transfer modeling of solar thermochemical systems, in particular for time-dependent analyses. Chemical kinetic models generally rely on experimental investigations to determine the rate constants in the model. The main factors that influence the reaction rate include the reaction temperature, the concentration of the reactants, the physical state of reactants, and the presence of catalysts. A complete kinetic modeling for inferring the rate constants requires coupling between a chemical kinetic model, conservation of species, and conservation of energy. Because kinetic analyses are complementary to heat transfer studies, we provide only a brief overview of this topic rather than its comprehensive review.

Several approaches exist to model the kinetics of high-temperature thermochemical reactions. In the most common approach, the focus is on a bulk kinetic reaction law and its calibration using experimental data. This approach does not attempt to model the microscale reaction mechanisms, which usually requires sophisticated computational chemistry techniques. The bulk kinetic reaction approach for modeling the reactor scale systems is described here. Experimental investigations of reaction kinetics are typically performed using thermogravimeters [64–72] or laboratory scale reactors, including fluidized beds [73–75], stabilized beds [76–78], and monolithic structured reactors [79–83]. Reaction kinetic modeling associated with each of these practices requires special attention to the corresponding experimental conditions. Some of the considerations are discussed below.

A general kinetic relation for heterogeneous reactions involving one reactive species can typically be represented by

$$r_j''' = k(T)f(x)C_j^n \tag{3}$$

where r_j''' is the rate of production or consumption of species j. The term $k(T) = k_0 \exp(-E_a/RT)$ is the temperature dependent term that follows the Arrhenius equation, n is the order of the reaction, k_0 is typically termed a reaction rate constant, E_a is the activation energy, R is the universal gas constant, T is temperature, $f(x)$ is a dimensionless function that depends on the reaction mechanism, x is the mass fraction of the reacted particles, and C_j is the molar concentration of species j. Since the molecular kinetic energy follows a Boltzmann distribution, one can expect the proportion of collisions with energy greater than E_a to vary with $\exp(-E_a/RT)$, which leads to the Arrhenius form of the reaction, where a very strong dependence on temperature is evident.

For monolithic reactors with small reactive surface area or small samples used in thermogravitometers the species concentration gradient across the sample is negligible due to the small amount of product gas produced as compared to the carrier gases. For such cases, the model given by Eq. (3) is sufficient to characterize the reactant output [65,68–70]. However, for larger scale reactors, such as fluidized or stabilized beds with large reactive surface area, the species concentration gradient is significant in the flow direction, and a control volume approach combined with Eq. (3) is needed to characterize the reactor output [77].

The functional form of $f(x)$ of Eq. (3) depends on the local reaction mechanism. Recently, Go et al. [67] categorized the available reaction mechanisms into three groups: diffusion controlled, boundary-controlled, and random nucleation models. Since the point at which the reaction mechanism changes behavior from one model to another is not clear, Mehdizadeh et al. [77] recently combined the contracting sphere and three-dimensional diffusion models into a single expression called the hybrid model.

The activation energy, reaction rate constant, and the reaction order can be found using either iterative or a direct methods. The direct method usually requires many experiments at different reaction temperatures and inlet concentrations. The iterative method usually requires a smaller number of experiments for calibration. For example, should experimental data be available for different reaction temperatures, an iterative method can be used. The kinetic rate given by Eq. (3) is highly dependent on the temperature and moderately dependent on the concentration. For the iterative method, it can be initially assumed that the reaction is first order and by varying $k(T)$ in Eq. (3) and solving the species transport equation, a curve fit matching the experimental data can be found. This can be repeated for different reaction temperatures. By plotting the logarithm of $k(T)$ versus $1/T$, the first estimate of the activation energy and reaction rate constant can be found from the slope and the intercept of the linear graph. In the next iteration, by knowing the activation energy and reaction rate constant and by varying the order of the reaction n, the new value of n can be found. Using the new value of n, the first procedure can be repeated to find a better estimate of the activation energy. Through this process, the quality of the curve fit can be iteratively improved [77].

For the direct method, there are usually two sets of experiments required. These include one for temperature variation at constant inlet concentration and another for inlet concentration variation at a constant reaction temperature. Using this method, the order of the reaction simply can be found by comparing the peak production rate.

In a recent study, the hydrogen production for a laboratory scale iron-based magnetically stabilized porous structure (MSPS) is experimentally investigated [76,77]. It has been recently demonstrated that the MSPS can significantly enhance the production of hydrogen using a two-step nonvolatile looping process [77]. The core idea is to utilize the magnetic property of iron particles in a

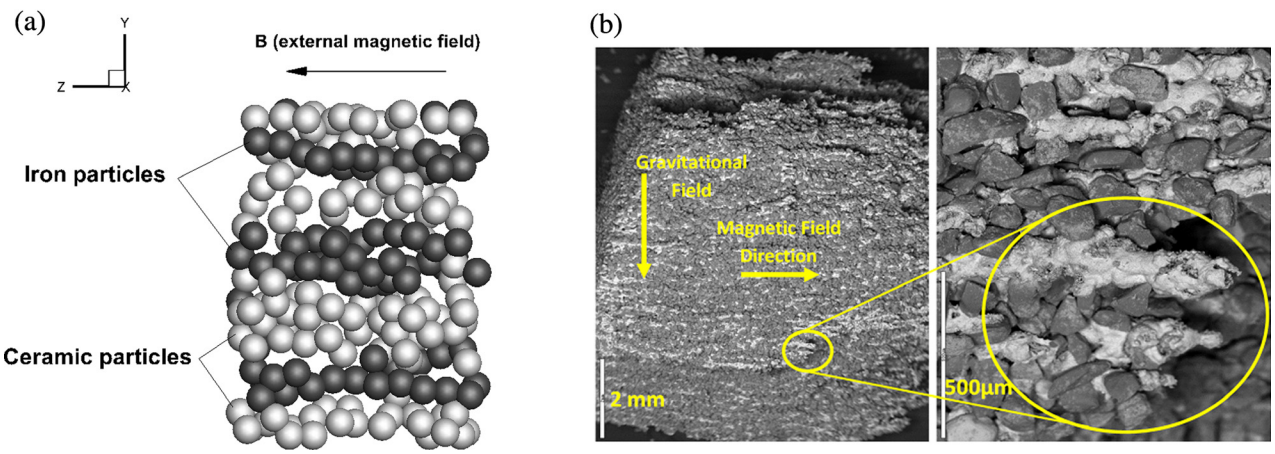

Fig. 9 (*a*) DES simulation of the formed MSPS in a uniform magnetic field [84], and (*b*) SEM image of MSPS after 11 redox cycles; darker particles are silica and sintered iron chains have lighter tone [76]. (Reproduced with permission from the International Association of Hydrogen Energy.)

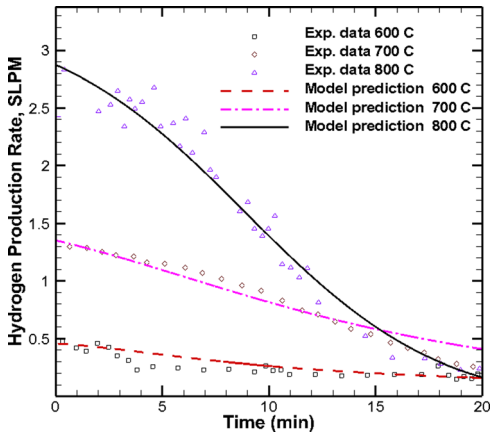

Fig. 10 Comparison of measured and predicted hydrogen production rates at different temperatures [77]. (Reproduced with permission from the International Association of Hydrogen Energy.)

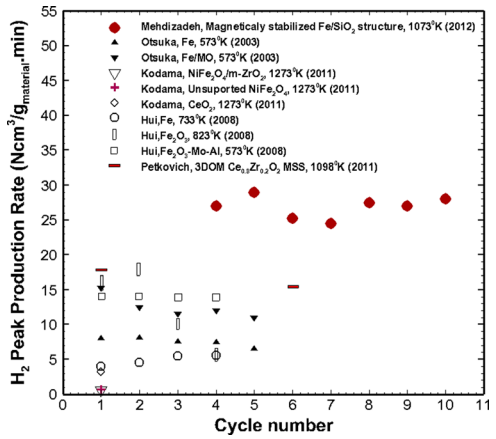

Fig. 11 Comparison of peak hydrogen production rates for repeated redox cycles using different reactive materials [28,76,85–87]

uniform external magnetic field to align iron particles in the form of many iron particle chains with the same polarity along the magnetic field lines. The chains with the same polarity repel each other and provide a natural spacing among neighboring chains, hence, substantially preserving the chemically active surface area around particles upon sintering process (nonhomogeneous and anisotropic sintering). The presence of the secondary ceramic particles (silica) in the structure enhances the porosity of the formed structure and creates a stable structure through consecutive oxidation/reduction cycles at high temperatures. Simulation results of the formed MSPS using discrete element simulation (DES) and SEM images of the MSPS are shown in Fig. 9 [76,84]. The hydrogen production rate measurements are used in the parametric study of the model to find the activation energy, order of the reaction, and the best form of the reaction rate model [77]. Figure 10 compares the model prediction with the experimental data for different reaction temperatures and shows good agreement. After validation, Mehdizadeh et al. [77] introduced a dimensionless parameter called the reactor effectiveness, and this parameter is utilized to find the operating conditions (time dependent inlet steam flow rate) for which the reactor effectiveness is the highest. The peak hydrogen production rate from the MSPS is almost double that of the best rate yet reported in the literature and shown in Fig. 11 [28,76,85–87]. The highly reactive MSPS is very suitable for solar thermochemical applications, and the model can provide an excellent tool for designing and controlling larger scale reactors.

5 Heat and Mass Transfer Modeling of Solar Thermochemical Systems

The basic approach to modeling coupled heat and mass transfer in reacting media of high-temperature solar thermochemical systems such as solar reactors and simplified setups exposed to concentrated solar radiation involves simultaneous solutions of Eq. (1) along with the mass, momentum, and energy conservation equations. Transient variation of radiative properties typical to such systems necessitates determination of the radiative contribution to the energy equation at any instant of the solution, leading to high computational cost. The complexity of solution further increases for systems for which gas radiation effects cannot be neglected, requiring application of accurate but computationally expensive spectral methods [35]. Developments of fast and accurate computational techniques to alleviate these difficulties are the research challenges in the field of computational radiative transfer. The Monte Carlo [88] and finite volume [89] techniques are promising approaches to solve Eq. (1), especially for complex three-dimensional geometries encountered in solar thermochemical systems [90]. Numerous thermal transport models of solar thermochemical systems have been reported in the literature, for both fuel and chemical producing processes. The models vary in complexity and purpose, from those elucidating the effects of radiation–chemistry coupling in simplified one-dimensional geometries and neglecting other thermal transport processes to broader approaches involving all heat transfer modes and fluid dynamics in geometries representative of actual solar thermochemical reactors. Below, selected examples of numerical analyses are discussed for gasification of carbonaceous materials and thermochemical dissociation of ZnO.

Figure 12 depicts the modeling schematics of three solar gasification reactor concepts, namely an indirectly irradiated packed-bed (Fig. 12(*a*)), directly irradiated vortex-flow (Fig. 12(*b*)), and indirectly irradiated entrained flow (Fig. 12(*c*)) [91]. The principal modes of heat transfer are indicated. The indirectly irradiated packed-bed solar reactor, Fig. 12(*a*), was modeled by considering radiative exchange in an enclosure and quasi-1D transient heat transfer in the reacting packed bed and cavity walls [6]. Validation was accomplished in terms of bed temperatures, reacted mass, and bed shrink rates by comparing numerically calculated values with experimental results obtained from tests of the steam-gasification of beech charcoal in an 8 kW prototype solar reactor. Above 1300 K, radiative transfer was the predominant mode of heat transport within the bed, producing a sevenfold increase in the effective thermal conductivity. Conditions were typical of an ablation regime, characterized by the heat transfer to the depth of the bed being the reaction rate-controlling mechanism. The directly irradiated vortex-flow solar reactor, Fig. 12(*b*), was modeled by means of a two-phase heat and mass transfer formulation for polydisperse suspensions of reacting particles, and solved by advanced Monte Carlo and finite volume techniques with smoothing and underrelaxation [92,93]. Validation was accomplished by comparing the numerically calculated temperatures, product compositions, and chemical conversions with the experimentally measured values obtained from testing a 5 kW solar reactor prototype in a high-flux solar furnace. Heating rates of 10^5 K s^{-1} were obtained as a result of the efficient radiative heat transfer. Transient radiative heat transfer was examined for a nonisothermal, nongray, absorbing, emitting, and Mie-scattering suspension of coal particles undergoing shrinking by endothermic gasification [94,95]. A numerical model that incorporates parallel filtered collision-based Monte Carlo, finite volume, and explicit Euler time integration techniques was formulated for solving the unsteady energy equation that couples the radiative heat flux with the chemical kinetics. It was found that radiation in the visible and near IR spectrum incident on a cloud of coal particles greater than 2.5 μm is more likely to be forward-scattered than absorbed, but the opposite is true as the particles shrink below 1.3 μm. The

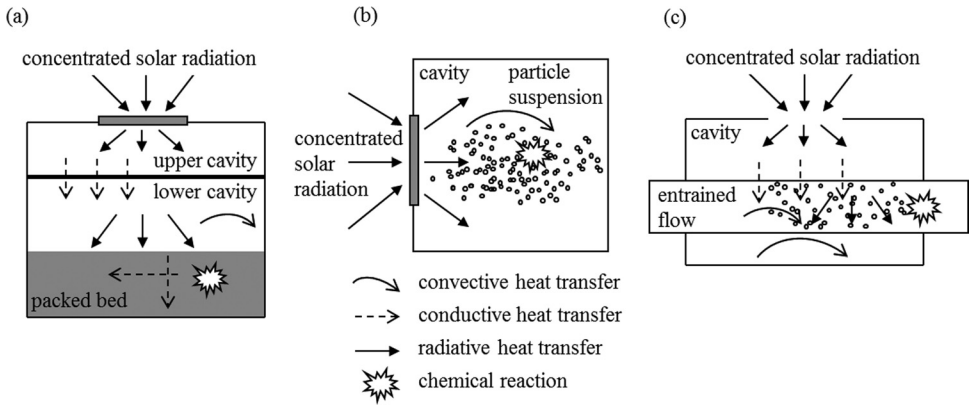

Fig. 12 Modeling schematics for the three solar reactor concepts [91]: (*a*) indirectly irradiated packed-bed, (*b*) directly irradiated vortex-flow, and (*c*) indirectly irradiated entrained flow. (Reproduced with permission from the Royal Society of Chemistry.)

medium becomes optically thinner as the particles shrink and this effect is more pronounced for smaller initial coal particles because these offer higher volume fractions to particle diameter ratios and, consequently, attain higher temperatures, reaction rates, and shrinking rates. A heat transfer numerical model was developed and experimentally validated for the steam-gasification of coal using a fluidized bed contained in a quartz tubular reactor that was directly exposed to concentrated thermal radiation [96]. Above 1450 K, the gas composition consisted of a nearly equimolar mixture of H_2 and CO, with less than 5% of CO_2. Heat was transferred to the particles predominantly by thermal radiation and to the gas by particle-gas convection since radiation absorption by particles was three orders of magnitude higher than that by the gas phase. The indirectly irradiated entrained-flow solar reactor, Fig. 12(*c*), was modeled using MC and radiosity methods to determine the radiation distribution within the cavity, which in turn was coupled to 2D conductive heat transfer through the reactor tube that drove convective and radiative heat transfer to the entrained reactive flow of shrinking particles [97,98].

Modeling the reactors for the solar thermochemical dissociation of ZnO has enabled a more comprehensive and in-depth understanding of the competing mechanisms and the identification of major sources of energy losses, which led to optimization and scaling up [99]. Various aspects of solar chemical reactors have been modeled at different levels of complexity. Computational fluid dynamics (CFD) was used to determine the flow patterns in a tubular aerosol flow reactor for aspect ratios between 0.15–0.45 at 1900–2,300 K [100]. The overall temperatures were found to decrease with increasing tube diameter, resulting in slower kinetics and lower ZnO-to-Zn conversions. Another CFD-based study for multitubular aerosol reactors allowed for the optimization of tube number, position, and dimensions for increased reactor efficiency [101]. CFD was also used to simulate the thermal reduction of metal oxides in particle-laden flows, including ZnO [102]. In a separate study, a cavity receiver containing a tubular absorber was coupled to a heat transfer model to predict temperatures and ZnO-to-Zn conversions [97]. A more fundamental approach was used to describe the transient radiative transfer of semitransparent ZnO particles undergoing thermal dissociation [103]. A diffusion-based approximate model for radiation heat transfer in a solar thermochemical reactor containing nonuniform ZnO particulate medium was developed in Ref. [104]. The effect of sintering and shrinkage on the rate of heat transfer was examined for a packed bed of ZnO particles subjected to $C = 1225–2{,}133$ suns and surface temperatures in the range 1834–2,109 K [71,72]. Operating conditions were typical of an ablation regime controlled by the rate of radiative heat transfer to the first layers of ZnO undergoing endothermic dissociation. This analysis served to determine the effective thermal transport properties of the ZnO packed bed, namely the extinction coefficient, the surface absorptivity, and the effective thermal conductivity. For simulating the rotary reactor, a heat transfer model was initially formulated [105,106] and then expanded to consider the exact 3D geometry of the cavity, the actual semibatch feeding mode of ZnO particles, and the fact that the packed-bed layer of ZnO particles lining the cavity shrinks as the reaction progresses

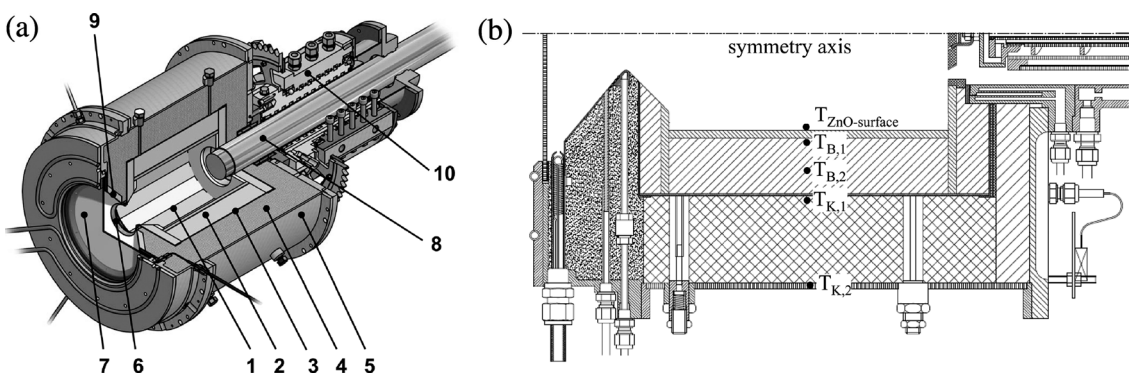

Fig. 13 Schematic of a solar chemical reactor for thermochemical dissociation of ZnO [21]: (*a*) reactor components: (1) rotating cavity lined with sintered ZnO tiles, (2) 80%Al_2O_3-20%SiO_2 insulation, (3) 95%Al_2O_3-5%Y_2O_3 CMC, (4) alumina fibers, (5) Al reactor mantle, (6) aperture, (7) quartz window, (8) dynamic feeder, (9) conical frustum, (10) rotary joint; (*b*) cross section of the solar chemical reactor. Indicated are the locations of temperature measurements with type-B (B) and type-K (K) thermocouples. (Reproduced with permission from Elsevier.)

[21]. The reactor configuration modeled in Ref. [21] is shown in Fig. 13. The more accurate kinetic rate law derived from experimental measurements in a solar-driven thermogravimeter for directly irradiated ZnO samples [70] was incorporated into the model. The radiosity and Monte Carlo methods were applied to obtain the distribution of net radiative fluxes, and the finite volume method with the explicit Euler time integration scheme were applied to solve the energy equation over a shrinking domain. Experimental validation was accomplished with a 10 kW reactor prototype in terms of temperatures and reaction extents for solar experimental runs with multiple feed-cycles (Fig. 14). The ZnO dissociation reaction occurred in the topmost layers, which is typical of an ablation regime, as radiative transfer to the endothermic reaction proceeded at a faster rate than heat conduction across the ZnO layer and the insulation. Scaling up the reactor to 100 and 1000 kW nominal solar power input has the potential of reaching maximum solar-to-chemical conversion efficiencies exceeding 50%, mainly as a result of higher reaction rates at higher operating temperatures and a reduction in the conduction losses through optimization of the geometry to minimize water-cooled components [21].

6 Thermal Measurements of Solar Thermochemical Systems

A key metric for the performance of a solar thermochemical reactor is the efficiency at which concentrated solar radiation is converted to fuel. The "sunlight-to-fuel" efficiency is defined as the solar energy stored in the fuel divided by all energy inputs to produce that fuel:

$$\eta_{\text{solar-to-fuel}} = \frac{\dot{m}_{\text{fuel}} \text{HHV}_{\text{fuel}}}{\dot{Q}_{\text{solar}} + \dot{Q}_{\text{parasitic}}} \tag{4}$$

where $\dot{m}_{\text{fuel}}$ is the fuel production rate, HHV is the higher heating value of the fuel, $\dot{Q}_{\text{solar}}$ is the input solar thermal power, and $\dot{Q}_{\text{parasitic}}$ is the equivalent parasitic thermal power, e.g., for preheating and separation processes, and material flow work. Care must be exercised when comparing reported efficiencies as various values of $\dot{Q}_{\text{solar}}$ are used. $\dot{Q}_{\text{solar}}$ is most often taken as the power at the aperture of the reactor and, thus, does not include optical losses in the collection and concentration optics. In addition, many reports of efficiency neglect the parasitic energy, which can be significant, particularly in prototype reactors that rely on high flow rates of preheated inert sweep gases.

Highly specialized facilities are used to measure the thermal and chemical behavior of reactive materials and prototype receiver/reactors. The solar thermogravimetric analyzer, or solar TGA, is a unique device to study the global kinetics of solid-state reactions in an environment similar to that expected in a solar reactor. As first described by Tabatabaie-Raissi et al. [68,69], the solar TGA is a directly irradiated, insulated cavity in which material samples are heated and reaction rates are determined from gravimetric measurements. They measured the kinetics of decomposition of zinc sulfate and pyrolysis of cellulose and discuss the necessity for accurate calibration and measurement of transient temperature and weight change. Schunk and Steinfeld [70] developed a solar TGA to study the kinetics of the solar thermal dissociation of zinc oxide. The device was used with a solar furnace capable of providing concentrated solar input up to 5000 suns. Temperatures were measured at the irradiated sample surface by pyrometry. By evaluating the reactive material under a range of conditions and numerically modeling these conditions at the macroscopic scale, they determined the effective thermal transport properties of the packed beds of ZnO at elevated temperature [71,72]. Note that solar TGAs are not standard laboratory equipment and may require specialized design to recreate the operating conditions expected in a particular solar thermochemical process or reactor.

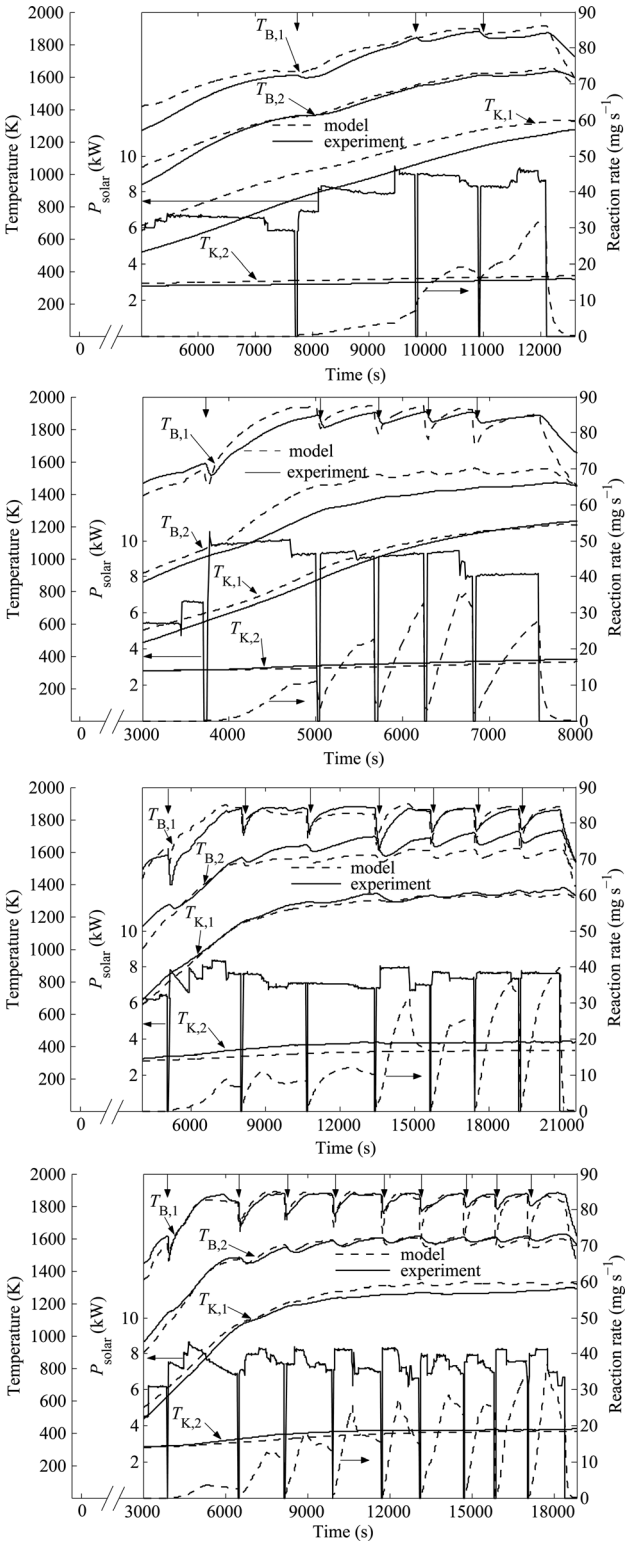

Fig. 14 Measured (solid curves) and computed (dashed curves) temperatures halfway along the reactor cavity at locations $T_{B,1}$, $T_{B,2}$, $T_{K,1}$, $T_{K,2}$ (see locations in Fig. 13(*b*)), measured radiation power input P_{solar}, and numerically calculated ZnO-dissociation rate as a function of time for a set of four experimental runs with (*a*) 3, (*b*) 5, (*c*) 7, and (*d*) 9 feed-cycles [21]. The top arrows point out to the times when the batch feeding of ZnO took place. (Reproduced with permission from Elsevier.)

Prototype reactors are routinely tested outdoors using solar furnaces and central-receiver testing facilities or indoors using high-flux solar simulators, in which an artificial radiative source approximates the spectral and directional characteristics of concentrated sunlight. Outdoor testing facilities are located in numerous research laboratories worldwide [107]. As an example, one of the largest solar furnaces is in Odeillo, France; the peak flux attained at the focus of the furnace over a ~1 cm diameter spot is 16 MW m^{-2}, which corresponds to a stagnation temperature in excess of 4000 K [108].

High-flux solar simulators use artificial radiation sources to replicate the spectral and directional attributes of commercial solar concentrators [109–112]. Most simulators use multiple radiation units each comprised of a high power (typically 6.5–7 kW_e) xenon arc lamp close-coupled to a precision reflector in the shape of a truncated ellipsoid. The xenon arc lamp has a short arc, which eliminates distortion, and has spectral characteristics representative of sunlight. Petrasch et al. [110] developed a Monte Carlo model to capture the effect of lamp and reflector geometry on flux distribution on an intended target plane, and Krueger et al. [111] presented a systematic analytical-numerical procedure to design a high-flux solar simulator, as well as insight into the impact of design parameters on the transfer efficiency of radiation from source to target and tradeoffs of total power and spatial distribution of the flux. The University of Minnesota solar simulator has seven radiation units and provides up to 9.2 kW over a 60 mm diameter circular area located in the focal plane, corresponding to an average flux of 3200 kW m^{-2}, with a peak flux of 7300 kW m^{-2} [112]. The largest simulator at the Paul Scherrer Institute uses an array of ten xenon short arc lamps and is capable of delivering 50 kW of radiative power onto a 24-cm diameter circular target with a peak flux in excess of 11,000 kW m^{-2} [110].

6.1 Radiative Flux Measurement. One of the major challenges in using solar simulators to evaluate reactors and material response to high-flux radiation is accurate measurement of the flux at the reactor aperture or at the surface of the material. A common approach to measuring two-dimensional flux distributions involves positioning a water-cooled Lambertian target in the measurement plane, while a charge coupled device (CCD) camera views the concentrated radiation reflected from the target through absorptive-reflective neutral density filters and a lens [113,114]. The radiative input to the camera is attenuated by filters to avoid saturating or damaging the CCD chip. The recorded array of grayscale values provides the basis for computing the spatial distribution of radiative flux incident on the target by employing a series of calibrations. The raw grayscale images are corrected for perspective distortion due to the angle with which the camera views the target, and the pixel size is related to the actual size of the target section that it represents. Additionally, the camera background signal is measured and subtracted from each flux image. The pixel grayscale value is related to incident radiative flux by a direct flux measurement, such as a circular foil heat flux gauge. One of the challenges in this approach is the calibration of the heat flux gauge considering the spectral characteristics of the absorptive coating [112,115–118]. Calibration errors of up to 30% are possible if the spectral content of the source used to calibrate the gauge differs from the spectral distribution of the applied light source. This issue arises because the colloidal graphite coating used in many gauges is not gray.

The directional characteristics of the concentrated radiation are typically predicted using ray tracing simulations. Erickson and Petrasch [118] developed an inverse approach to identify the directional and spatial intensity distributions from multiple parallel flux measurements at varying distances from the focal plane. The method was successfully validated for two-dimensional parabolic and elliptical troughs concentrating systems.

6.2 Temperature Measurement—Contact Sensors. The coupled, multimode, and rapid heat transfer in solar thermochemical processes calls for specialized techniques to measure temperature accurately. High-temperature measurement probes are typically alumina sheathed type-B, R, or S thermocouple sensors. As in all high-temperature measurements, conduction along the probe, radiation exchange with the surroundings, and contact resistance must be accounted for in converting the raw data to an accurate estimate of measured temperature. Additionally, due to the rapid heating and cooling rates (i.e., from solar furnaces, solar simulators, or benchtop-scale imaging furnaces), errors due to sensor time lag are often significant [68,69]. The time constant is not known a priori in radiative systems and, thus, must be measured in a carefully designed experiment that replicates the heat transfer modes in the planned operational environment.

Based on recent measurements of the temperature of a solid ceria powder, which was rapidly heated and cooled between 1000 and 1800 K, a first-order dynamic model is sufficient to correct for the response of a Pt/Pt-Rh (type R) sheathed thermocouple despite nonlinearities in heat transfer. The solid powder was held in an alumina tube and heated by an infrared imaging furnace. The 24

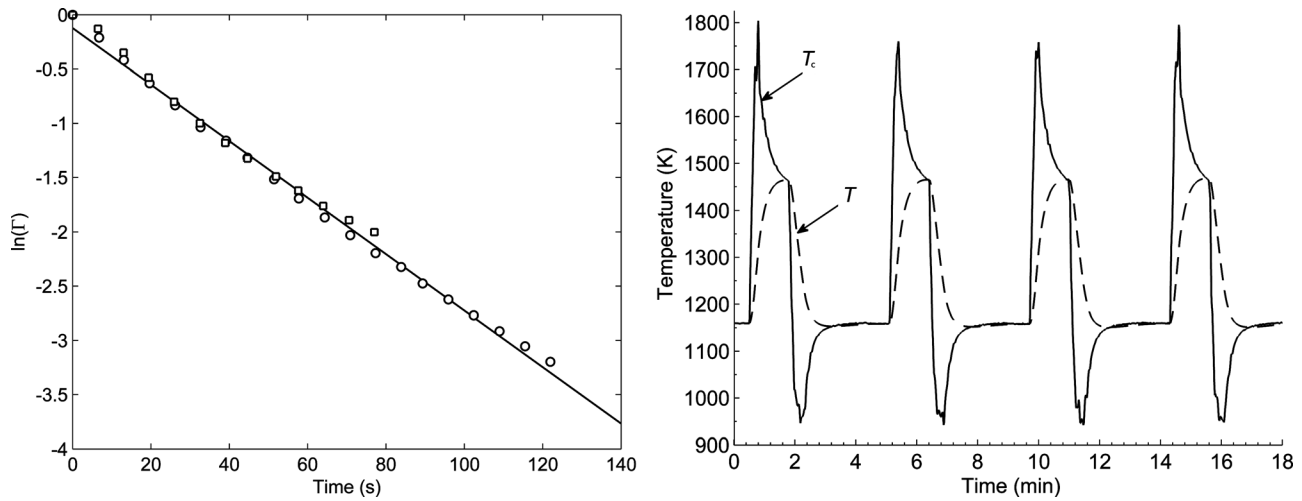

Fig. 15 (*a*) The error fraction of the response of the alumina-sheathed Pt/Pt-Rh thermocouple probe to a step change in temperature in a highly radiative (IR) environment. The first-order time constant is extracted from the linear regression. (*b*) The uncorrected (T) and corrected (T_c) temperature of the solid powder during rapid heating and cooling cycles, demonstrating the importance of correcting for the sluggish response of the temperature probe.

gauge Pt/Pt-Rh thermocouple was embedded in a 4.76 mm diameter alumina sheath and placed in contact with the powder. The time constant was measured in a separate experiment in the furnace but without the powder. With the furnace held at a fixed power output so that the tube was thermally equilibrated, the temperature probe was plunged into the hottest region of the tube, and rapidly heated to a new steady-state temperature. Figure 15(*a*) shows the response of the probe. The time constant, as determined from a linear regression, is 38 s. The corrected T_c and uncorrected T temperatures are shown in Fig. 15(*b*). When the furnace power is increased to rapidly heat the powder, the uncorrected temperature rises at a maximum rate of $\sim$800 K min^{-1}. The corrected temperature shows that the heating rate is 2000 K min^{-1}. The maximum uncorrected temperature is 1470 K and the maximum corrected temperature is $\sim$1800 K. Similar to the overshoot error during heating, an undershoot error is incurred during cooling. The difference between the minimum uncorrected temperature and the minimum corrected temperature is $\sim$200 K.

Increased errors in temperature measurements with contact sensors also result from the direct irradiation of the sensor in thermal radiating environments such as solar thermochemical reactors. Experimental and analytical correction techniques are employed to minimize this effect. A combined experimental-analytical methodology involving a suction thermocouple apparatus and associated heat transfer model for determining gas temperature from shielded thermocouple readings by radiation, convection and conduction dimensionless correlations was developed in Ref. [119]. The apparatus and methodology were calibrated and applied to measure gas flow temperatures in a tubular furnace with wall temperatures up to 1223 K. Results were compared with predictions by CFD simulations.

6.3 Temperature Measurement—Pyrometers. Pyrometry temperature measurements are based on the thermal emission from a surface and are commonly employed in the fields of concentrating solar, gas turbines, metallurgy, and surface processing [120–129]. It offers the advantages that the sensor is outside the harsh measurement environment and has rapid time response. It is limited to the measurement of surface temperature since gases are not strong emitters at the temperatures typically encountered in solar reactors. The radiation streaming from a surface, the radiosity J_λ, detected by a pyrometer consists of both thermal emission $\varepsilon_\lambda E_{b,\lambda}$ and reflection $\rho_\lambda G_\lambda$:

$$J_\lambda = \varepsilon_\lambda E_{b,\lambda} + \rho_\lambda G_\lambda \tag{5}$$

These two contributions to the radiosity must be decoupled since the temperature of the surface is related only to the emitted part of the radiation through the Planck distribution for a blackbody $E_{b,\lambda}$. The reflected radiation includes the concentrated radiation delivered to the solar reactor, either from a solar furnace or a solar simulator, and also emitted radiation from other high-temperature surfaces in view of the surface of interest. In solar furnaces, three methods have been developed for decoupling the emitted and reflected parts of the radiosity: flash assisted multiwavelength pyrometry (FAMP) [121,130–132], pyroreflectometry [133–135], and solar-blind pyrometry [121,123–127,136]. An advantage of FAMP and pyroreflectometry is that, in addition to decoupling thermal emission from the surface radiosity, the emissivity of the surface ε_λ is measured in situ. A disadvantage of the methods is that both require continuous sampling of the radiation from a cold reference target of known reflectivity.

The most common approach to radiation-based temperature measurement in solar reactors is solar-blind pyrometry, which takes advantage of the natural attenuation of certain bandwidths in the solar radiation spectrum by water vapor and carbon dioxide in the atmosphere [121,126,127]. Bandpass filters are placed in the line of sight between the radiation sensor and the surface of interest that allow only the atmosphere attenuated wavelengths of radiation to enter the sensor so that the radiation arriving at the sensor is solely the result of thermal emission from the surface [123–125]. The emissivity of the surface of interest must be known in order to calculate the temperature from the measured radiation. Alternatively, the emissivity can be estimated based on measurements from multiple solar-blind pyrometers [136].

Solar-blind pyrometry cannot be used in a solar simulator because there is no attenuation by water and carbon dioxide in the atmosphere [137]. Pyroreflectometry and FAMP can be used in a simulator but accuracy is reduced by corrections required because the spectral content of the light at the focal plane depends on the point of origin at the arc [138]. Alxneit has demonstrated a new pyrometric method for solar simulators based on modulating the output of the arc lamps at frequencies up to a few hundred hertz. The approach is based on the idea that the thermal time response of the surface whose temperature is being measured is slower than the rate at which the arc lamp output is modulated. Thus, the thermal emission of the surface is steady in time, while the reflected radiation from the surface exhibits the imposed oscillations, and the steady thermal emission can be decoupled from the oscillatory radiosity. This approach has been applied for the case of a single arc lamp, and the techniques required to adapt it to a simulator consisting of multiple lamps are under development [137].

7 Summary

Solar thermochemical processes make use of concentrated solar radiation for driving chemical reactions. The processes are classified into those for production of solar fuels and chemical commodities. Solar thermochemical reactors implementing them operate at high temperatures, typically above 1000 K. Understanding heat and mass transfer phenomena and mechanisms of chemical reactions is crucial to the design of efficient reactors. Heat and mass transfer characterization of heterogeneous reacting media, formulation of accurate kinetic rate equations, modeling of combined heat and mass transfer in heterogeneous reacting media, and accurate measurements of radiative fluxes and temperatures in high-temperature reacting systems are of fundamental importance for advancements of solar thermochemical reactor technology for efficient solar-to-chemical energy conversion.

Nomenclature

C_j = molar concentration of species j, mol m^{-3}
E_λ = spectral hemispherical emissive power, W m$^{-2}\mu$m^{-1}
E_a = activation energy, J mol^{-1}
f = conversion function; tortuosity
G_λ = spectral direction-integrated intensity, W m$^{-2}\mu$m^{-1}
HHV = higher heating value of fuel, J kg^{-1}
I = spectral radiative intensity, W m$^{-2}\mu$m^{-1} sr^{-1}
J_λ = spectral hemispherical radiosity, W m$^{-2}\mu$m^{-1}
k_0 = reaction rate constant, (m^3 mol^{-1})$^{n-1}$ s^{-1}
n = reaction order
Pr = Prandtl number
$\vec{\mathbf{q}}''$ = heat flux vector
R = universal gas constant, J mol^{-1} K^{-1}
$\vec{\mathbf{r}}$ = position vector
Re = Reynolds number
r_j''' = rate of production, mol m^{-3}s^{-1}
s = path length, m
$\hat{\mathbf{s}}$ = direction unit vector
T = temperature, K
x = mass fraction of reacted particles

Greek Symbols

β = extinction coefficient, m^{-1}
ε = porosity

η = efficiency
κ = absorption coefficient, m^{-1}
λ = radiation wavelength, μm
σ_s = scattering coefficient, m^{-1}
τ = tortuosity
Φ = scattering phase function
Ω = solid angle, sr

Subscripts

b = blackbody
in = incoming
j = species
parasitic = parasitic power input
solar = incident solar radiation
λ = spectral
0 = initial

Abbreviations

CT = computed tomography
DPLS = direct pore-level numerical simulations
RPC = reticulate porous ceramic

References

[1] Fletcher, E. A., 2001, "Solarthermal Processing: A Review," ASME J. Sol. Energy Eng., **123**(2), pp. 63–74.
[2] Kodama, T., 2003, "High-Temperature Solar Chemistry for Converting Solar Heat to Chemical Fuels," Prog. Energ. Combust. Sci., **29**, pp. 567–597.
[3] Steinfeld, A., and Palumbo, R., 2001, "Solar Thermochemical Process Technology," *Encyclopedia of Physical Science and Technology*, Vol. 15, R. A. Meiers, ed., Academic Press, San Diego, pp. 237–256.
[4] Hirsch, D., Epstein, M., and Steinfeld, A., 2001, "The Solar Thermal Decarbonization of Natural Gas," Int. J. Hyd. Energ., **26**, pp. 1023–1033.
[5] Dahl, J. K., Weimer, A. W., Lewandowski, A., Bingham, C., Brütsch, F., and Steinfeld, A., 2004, "Dry Reforming of Methane Using a Solar-Thermal Aerosol Flow Reactor," Ind. Eng. Chem. Res., **43**, pp. 5489–5495.
[6] Piatkowski, N., and Steinfeld, A., 2008, "Solar-Driven Coal Gasification in a Thermally Irradiated Packed-Bed Reactor," Energ. Fuel., **22**, pp. 2043–2052.
[7] Hathaway, B. J., Davidson, J. H., and Kittelson, D. B., 2011, "Solar Gasification of Biomass: Kinetics of Pyrolysis and Steam Gasification in Molten Salt," ASME J. Sol. Energy Eng., **133**(2), p. 021011.
[8] Tamaura, Y., Kojima, M., Hasegawa, N., Tsuji, M., Ehrensberger, K., and Steinfeld, A., 1997, "Solar Energy Conversion Into H_2 Energy Using Ferrites," J. Phys. IV, **7**, pp. 673–674.
[9] Steinfeld, A., 2002, "Solar Hydrogen Production via a 2-Step Water-Splitting Thermochemical Cycle Based on Zn/ZnO Redox Reactions," Int. J. Hyd. Energ., **27**, pp. 611–619.
[10] Chueh, W. C., and Haile, S. M., 2009, "Ceria as a Thermochemical Reaction Medium for Selectively Generating Syngas or Methane From H_2O and CO_2," ChemSusChem, **2**, pp. 735–739.
[11] Alvani, C., Bellusci, M., La Barbera, A., Padella, F., Pentimalli, M., Seralessandri, L., and Varsano, F., 2009, "Reactive Pellets for Improved Solar Hydrogen Production Based on Sodium Manganese Ferrite Thermochemical Cycle," ASME J. Sol. Energy Eng., **131**(3), p. 031015.
[12] Fresno, F., Yoshida, T., Gokon, N., Fernandez-Saavedra, R., and Kodama, T., 2010, "Comparative Study of the Activity of Nickel Ferrites for Solar Hydrogen Production by Two-Step Thermochemical Cycles," Int. J. Hyd. Energ., **35**, pp. 8503–8510.
[13] Kogan, A., 2000, "Direct Solar Thermal Splitting of Water and On-Site Separation of the Products—IV. Development of Porous Ceramic Membranes for a Solar Thermal Water-Splitting Reactor," Int. J. Hyd. Energ., **25**, pp. 1043–1050.
[14] Meier, A., Bonaldi, E., Cella, G. M., Lipiński, W., and Wuillemin, D., 2006, "Solar Chemical Reactor Technology for Industrial Production of Lime," Solar Energ., **80**, pp. 1355–1362.
[15] Gálvez, M. E., Halmann, M., and Steinfeld, A., 2007, "Ammonia Production via a Two-Step Al_2O_3/AlN Thermochemical Cycle. 1. Thermodynamic, Environmental, and Economic Analyses," Ind. Eng. Chem. Res., **46**, pp. 2042–2046.
[16] Schaffner, B., Hoffelner, W., and Steinfeld, A., 2000, "Recycling of Hazardous Solid Waste Material Using High-Temperature Solar Process Heat. 1. Thermodynamic Analysis," Environ. Sci. Tech., **34**, pp. 4177–4184.
[17] Matthews, L., and Lipiński, W., 2012, "Thermodynamic Analysis of Solar Thermochemical CO_2 Capture via Carbonation/Calcination Cycle With Heat Recovery," Energy, **45**, pp. 900–907.
[18] Palumbo, R., Keunecke, M., Möller, S., and Steinfeld, A., 2004, "Reflections on the Design of Solar Thermal Chemical Reactors: Thoughts in Transformation," Energy, **29**, pp. 727–744.
[19] Mischler, D., and Steinfeld, A., 1995, "Nonisothermal Nongray Absorbing-Emitting-Scattering Suspension of Fe_3O_4 Particles Under Concentrated Solar Irradiation," ASME J. Heat Transfer, **117**(2), pp. 346–354.
[20] Von Zedtwitz, P., and Steinfeld, A., 2005, "Steam-Gasification of Coal in a Fluidized-Bed/Packed-Bed Reactor Exposed to Concentrated Thermal Radiation—Modeling and Experimental Validation," Ind. Eng. Chem. Res., **44**, pp. 3852–3861.
[21] Schunk, L. O., Lipiński, W., and Steinfeld, A., 2009, "Heat Transfer Model of a Solar Receiver-Reactor for the Thermal Dissociation of ZnO—Experimental Validation at 10 kW and Scale-Up to 1 MW," Chem. Eng. J., **150**, pp. 502–508.
[22] Chueh, W. C., Falter, C., Abbott, M., Scipio, D., Furler, P., Haile, S. M., and Steinfeld, A., 2010, "High-Flux Solar-Driven Thermochemical Dissociation of CO_2 and H_2O Using Nonstoichiometric Ceria," Science, **330**, pp. 1797–1801.
[23] Wyss, J., Martinek, J., Kerins, M., Dahl, J. K., Weimer, A., Lewandowski, A., Bingham, C., 2007, "Rapid Solar-Thermal Decarbonization of Methane in a Fluid-Wall Aerosol Flow Reactor: Fundamentals and Application," Int. J. Chem. React. Eng., **5**, p. A69.
[24] Kaviany, M., 2008, *Heat Transfer Physics*, Cambridge University Press, Cambridge.
[25] Zhang, Z. M., 2007, *Nano/Microscale Heat Transfer*, McGraw-Hill, New York.
[26] Chen, G., 2005, *Nanoscale Energy Transport and Conversion: A Parallel Treatment of Electrons, Molecules, Phonons, and Photons*, Oxford University Press, Oxford.
[27] Kaviany, M., 1995, *Principles of Heat Transfer in Porous Media*, Springer-Verlag, New York.
[28] Petkovich, N. D., Rudisill, S. G., Venstrom, L. J., Boman, D. B., Davidson, J. H., and Stein, A., 2011, "Control of Heterogeneity in Nanostructured $Ce_{1-x}Zr_xO_2$ Binary Oxides for Enhanced Thermal Stability and Water Splitting Activity," J. Phys. Chem., **115**, pp. 21022–21033.
[29] Akolkar, A., and Petrasch, J., 2011, "Tomography Based Pore-Level Optimization of Radiative Transfer in Porous Media," Int. J. Heat Mass Tran., **54**, pp. 4775–4783.
[30] Akolkar, A., and Petrasch, J., 2012, "Tomography-Based Characterization and Optimization of Fluid Flow Through Porous Media," Transp. Porous Med., **95**, pp. 535–550.
[31] Norton, W. H., 1993, *The Norton History of Chemistry*, W.W. Norton, New York.
[32] Trombe, F., and Foex, M., 1951, "Essai de Metallurgie du Chrome par l'Hydrogene au Four Solaire," Rev. Metall., **48**, pp. 359–362.
[33] Nakamura, T., 1977, "Hydrogen Production From Water Utilizing Solar Heat at High Temperatures," Solar Energ., **19**, pp. 467–475.
[34] Fletcher, E. A., and Moen, R. L., 1977, "Hydrogen and Oxygen From Water," Science, **197**, pp. 1050–1056.
[35] Modest, M. F., 2003, *Radiative Heat Transfer*, 3rd ed., Academic Press, Amsterdam.
[36] Haussener, S., Lipiński, W., Petrasch, J., Wyss, P., and Steinfeld, A., 2009, "Tomographic Characterization of a Semitransparent-Particle Packed Bed and Determination of Its Thermal Radiative Properties," ASME J. Heat Transfer, **131**(7), p. 072701.
[37] Lipiński, W., Petrasch, J., and Haussener, S., 2010, "Application of the Spatial Averaging Theorem to Radiative Heat Transfer in Two-Phase Media," J. Quant. Spectrosc. Rad. T., **111**, pp. 253–258.
[38] Lipiński, W., Keene, D., Haussener, S., and Petrasch, J., 2010, "Continuum Radiative Heat Transfer Modeling in Media Consisting of Optically Distinct Components in the Limit of Geometrical Optics," J. Quant. Spectrosc. Rad. T., **111**, pp. 2474–2480.
[39] Baillis, D., and Sacadura, J.-F., 2000, "Thermal Radiation Properties of Dispersed Media: Theoretical Prediction and Experimental Characterization," J. Quant. Spectrosc. Rad. T., **67**, pp. 327–363.
[40] Agarwal, B. M., and Mengüç, M., 1991, "Forward and Inverse Analysis of Single and Multiple Scattering of Collimated Radiation in an Axisymmetric System," Int. J. Heat Mass Tran., **34**, pp. 633–647.
[41] Osinga, T., Frommherz, U., Steinfeld, A., and Wieckert, C., 2004, "Experimental Investigation of the Solar Carbothermic Reduction of ZnO Using a Two-Cavity Solar Reactor," ASME J. Sol. Energy Eng., **126**(1), pp. 633–637.
[42] Osinga, T., Lipiński, W., Guilot, E., Olalde, G., and Steinfeld, A., 2006, "Experimental Determination of the Extinction Coefficient for a Packed-Bed Particulate Medium," Exp. Heat Trans., **19**, pp. 69–79.
[43] Lipiński, W., Guillot, E., Olalde, G., and Steinfeld, A., 2008, "Transmittance Enhancement of Packed-Bed Particulate Media," Exp. Heat Trans., **21**, pp. 73–82.
[44] Jäger, K., Lipiński, W., Katzgraber, H. G., and Steinfeld, A., 2009, "Determination of Thermal Radiative Properties of Packed-Bed Media Containing a Mixture of Polydispersed Particles," Int. J. Therm. Sci., **48**, pp. 1510–1516.
[45] Coray, P., Lipiński, W., and Steinfeld, A., 2011, "Spectroscopic Goniometry System for Determining Thermal Radiative Properties of Participating Media," Exp. Heat Trans., **24**, pp. 300–312.
[46] Coray, P., Petrasch, J., Lipiński, W., and Steinfeld, A., 2007, "Determination of Radiative Characteristics of Reticulate Porous Ceramics," M. P. Mengüç, and N. Selçuk, eds., Proceedings of the 5th International Symposium on Radiative Transfer RAD-V, Bodrum, Turkey, June 17–22.
[47] Coray, P., Lipiński, W., and Steinfeld, A., 2010, "Experimental and Numerical Determination of Thermal Radiative Properties of ZnO Particulate Media," ASME J. Heat Transfer, **132**(1), p. 012701.

[48] Liang, Z., Chueh, W. C., Ganesan, K., Haile, S. M., and Lipiński, W., 2011, "Experimental Determination of Transmittance of Porous Cerium Dioxide Media in the Spectral Range 300–1,100 nm," Exp. Heat Trans., **24**, pp. 285–299.
[49] Ganesan, K., and Lipiński, W., 2011, "Experimental Determination of Spectral Transmittance of Porous Cerium Dioxide in the Range 900–1700 nm," ASME J. Heat Transfer, **133**(10), p. 104501.
[50] Dombrovsky, L., Ganesan, K., and Lipiński, W., 2012, "Combined Two-Flux Approximation and Monte Carlo Model for Identification of Radiative Properties of Highly Scattering Dispersed Materials," Comput. Therm. Sci., **4**, pp. 365–378.
[51] Ganesan, K., Dombrovsky, L. A., and Lipiński, W., 2013, "Visible and Near-Infrared Optical Properties of Ceria Ceramics," Infrared Phys. Techn., **57**, pp. 101–109.
[52] Berryman, J., and Blair, S., 1986, "Use of Digital Image Analysis to Estimate Fluid Permeability of Porous Material: Application of Two-Point Correlation Functions," J. Appl. Phys., **60**, pp. 1930–1938.
[53] Rintoul, M., Torquato, S., Yeong, C., Keane, D., Erramilli, S., Jun, Y., Dabbs, D., and Aksay, I., 1996, "Structure and Transport Properties of a Porous Magnetic Gel via X-ray Microtomography," Phys. Rev. E, **54**, pp. 2663–2669.
[54] Tancrez, M., and Taine, J., 2004, "Direct Identification of Absorption and Scattering Coefficients and Phase Function of a Porous Medium by a Monte Carlo Technique," Int. J. Heat Mass Tran., **47**, pp. 373–383.
[55] Zeghondy, B., Iacona, E., and Taine, J., 2006, "Determination of the Anisotropic Radiative Properties of a Porous Material by Radiative Distribution Function Identification (RDFI)," Int. J. Heat Mass Tran., **49**, pp. 2810–2819.
[56] Petrasch, J., Wyss, P., and Steinfeld, A., 2007, "Tomography-Based Monte Carlo Determination of Radiative Properties of Reticulate Porous Ceramics," J. Quant. Spectrosc. Ra., **105**, pp. 180–197.
[57] Petrasch, J., Wyss, P., Stämpfli, R., and Steinfeld, A., 2008, "Tomography-Based Multiscale Analyses of the 3D Geometrical Morphology of Reticulated Porous Ceramics," J. Am. Ceram. Soc., **91**, pp. 2659–2665.
[58] Petrasch, J., Schrader, B., Wyss, P., and Steinfeld, A., 2008, "Tomography-Based Determination of the Effective Thermal Conductivity of Reticulate Porous Ceramics," ASME J. Heat Transfer, **103**(3), p. 032602.
[59] Petrasch, J., Meier, F., Friess, H., and Steinfeld, A., 2008, "Tomography Based Determination of Permeability, Dupuit–Forchheimer Coefficient, and Interfacial Heat Transfer Coefficient in Reticulate Porous Ceramics," Int. J. Heat Fluid Flow, **29**, pp. 315–326.
[60] Haussener, S., Coray, P., Lipiński, W., Wyss, P., and Steinfeld, A., 2010, "Tomography-Based Heat and Mass Transfer Characterization of Reticulate Porous Ceramics for High-Temperature Processing," ASME J. Heat Transfer, **132**(2), p. 023305.
[61] Haussener, S., Lipiński, W., Wyss, P., and Steinfeld, A., 2010, "Tomography-Based Analysis of Radiative Transfer in Reacting Packed Beds Undergoing a Solid-Gas Thermochemical Transformation," ASME J. Heat Transfer, **132**(6), p. 061201.
[62] Haussener, S., Jerjen, I., Wyss, P., and Steinfeld, A., 2012, "Tomography-Based Determination of Effective Transport Properties for Reacting Porous Media," ASME J. Heat Transfer, **134**(1), p. 012601.
[63] Haussener, S., and Steinfeld, A., 2012, "Effective Heat and Mass Transport Properties of Anisotropic Porous Ceria for Solar Thermochemical Fuel Generation," Materials, **5**, pp. 192–209.
[64] Abanades, S., and Villafan-Vidales, H. I., 2011, "CO_2 and H_2O Conversion to Solar Fuels via Two-Step Solar Thermochemical Looping Using Iron Oxide Redox Pair," Chem. Eng. J., **175**, pp. 368–375
[65] Abanades, S., and Le Gal, A., 2012, "CO_2 Splitting by Thermo-Chemical Looping Based on $Zr_xCe_{1-x}O_2$ Oxygen Carriers for Synthetic Fuel Generation," Fuel, **102**, pp. 180–186.
[66] Chiron, F.-X., and Patience, G. S., 2012, "Kinetics of Mixed Copper–Iron Based Oxygen Carriers for Hydrogen Production by Chemical Looping Water Splitting," Int. J. Hyd. Energ., **37**, pp. 10526–10538.
[67] Go, K. S., Son, S. E., and Kim, S. D., 2008, "Reaction Kinetics of Reduction and Oxidation of Metal Oxides for Hydrogen Production," Int. J. Hyd. Energ., **33**, pp. 5986–5995.
[68] Tabatabaie-Raissi, A., Narayan, R., Mok, W. S. L., and Antal, J., Jr., 1989, "Solar Thermal, Decomposition Kinetics of Zinc Sulfate at High Heating Rates," Indust. Eng. Chem. Res., **28**, pp. 355–362.
[69] Tabatabaie-Raissi, A., Mok, W. S. L., and Antal, J., Jr., 1989, "Cellulose Pyrolysis Kinetics in a Simulated Solar Environment," Indust. Eng. Chem. Res., **28**, pp. 856–865.
[70] Schunk, L. O., and Steinfeld, A., 2009, "Kinetics of the Thermal Dissociation of ZnO Exposed to Concentrated Solar Irradiation Using a Solar-Driven Thermogravimeter in the 1800–2100 K Range," AIChe J., **55**, pp. 1497–1504.
[71] Dombrovsky, L., Schunk, L., Lipiński, W., and Steinfeld, A., 2009, "An Ablation Model for the Thermal Decomposition of Porous Zinc Oxide Layer Heated by Concentrated Solar Radiation," Int. J. Heat Mass Tran., **52**, pp. 2444–2452.
[72] Schunk, L. O., Lipiński, W., and Steinfeld, A., 2009, "Ablative Heat Transfer in a Shrinking Packed-Bed of ZnO Undergoing Solar Thermal Dissociation," AIChE J., **55**, pp. 1659–1659.
[73] Chen, S., Shi, Q., Xue, Z., Sun, X., and Xiang, W., 2011, "Experimental Investigation of Chemical-Looping Hydrogen Generation Using Al_2O_3 or TiO_2-Supported Iron Oxides in a Batch Fluidized Bed," Int. J. Hyd. Energ., **36**, pp. 8915–8926.
[74] Rydén, M., and Arjmand, M., 2012, "Continuous Hydrogen Production via the Steam–Iron Reaction by Chemical Looping in a Circulating Fluidized-Bed Reactor," Int. J. Hyd. Energ., **37**, pp. 4843–4854.
[75] Singh, A., Al-Raqom, F., Klausner, J. F., and Petrasch, J., 2012, "Production of Hydrogen via an Iron/Iron Oxide Looping Cycle: Thermodynamic Modeling and Experimental Validation," Int. J. Hyd. Energ., **37**, pp. 7442–7450.
[76] Mehdizadeh, M. A., Klausner, J. F., Mei, R., and Barde, A., 2012, "Enhancement of Thermochemical Hydrogen Production Using an Iron-Silica Magnetically Stabilized Porous Structure," Int. J. Hyd. Energ., **37**, pp. 8954–8963.
[77] Mehdizadeh, A. M., Klausner, J. F., Barde, A., Rahmatian, N., and Mei, R., 2012, "Investigation of Hydrogen Production Reaction Kinetics for an Iron-Silica Magnetically Stabilized Porous Structure," Int. J. Hyd. Energ., **37**, pp. 13263–13271.
[78] Stamatiou, A., Loutzenhiser, P. G., and Steinfeld, A., 2012, "Syngas Production From H_2O and CO_2 Over Zn Particles in a Packed-Bed Reactor," AIChE J., **58**, pp. 625–631.
[79] Agrafiotis, C., Roeb, C., Konstandopoulos, A. G., Nalbandian, L., Zaspalis, V. T., Sattler, C., Stobbe, P., and Steele, A. M., 2005, "Solar Water Splitting for Hydrogen Production With Monolithic Reactors," Solar Energ., **79**, pp. 409–421.
[80] Roeb, M., Neises, M., Säck, J.-P., Rietbrock, P., Monnerie, N., Dersch, J., Schmitz, M., and Sattler, C., 2009, "Operational Strategy of a Two-Step Thermochemical Process for Solar Hydrogen Production," Int. J. Hyd. Energ., **34**, pp. 4537–4545.
[81] Roeb, M., Säck, J.-P., Rietbrock, P., Prahl, C., Schreiber, H., Neises, M., De Oliveira, L., Graf, D., Ebert, M., Reinalter, W., Meyer-Grünefeldt, M., Sattler, C., Lopez, A., Vidal, A., Elsberg, A., Stobbe, P., Jones, D., Steele, A., Lorentzou, S., Pagkoura, C., Zygogianni, Z., Agrafiotis, C., and Konstandopoulos, A. G., 2011, "Test Operation of a 100 kW Pilot Plant for Solar Hydrogen Production From Water on a Solar Tower," Solar Energ., **85**, pp. 634–644.
[82] Furler, P., Scheffe, J. R., and Steinfeld, A., 2012, "Syngas Production by Simultaneous Splitting of H_2O and CO_2 via Ceria Redox Reactions in a High-Temperature Solar Reactor," Energ. Environ. Sci., **5**, pp. 6098–6103.
[83] Stehle, R. C., Bobek, M. M., Hooper, R., and Hahn, D. W., 2011, "Oxidation Reaction Kinetics for the Steam-Iron Process in Support of Hydrogen Production," Int. J. Hyd. Energ., **36**, pp. 15125–15135.
[84] Klausner, J. F., Hahn, D. W., Petrasch, J., Mei, R., Mehdizadeh, A. M., Barde, A., Allen, K., Rahmatian, N., Stehle, R. C., Bobek, S. M., Al-Raqom, F., Greek, B., Li, L., Abhishek, S., and Takagi, M., 2010, "Novel Magnetically Fluidized Bed Reactor Development for the Looping Process: Coal to Hydrogen Production R&D," DOE NETL Quarterly Report 6, Project DE-FE0001321.
[85] Hui, W., Xiaoqiong, F., Xiaofang, W., Sanping, C., and Shengli, G., 2008, "Hydrogen Production by Redox of Bimetal Cation-Modified Iron Oxide," Int. J. Hyd. Energ., **33**, pp. 7122–7128.
[86] Kodama, T., Imaizumi, N., Gokon, N., Hatamachi, T., Aoyagi, D., and Kondo, K., 2011, "Comparison Studies of Reactivity on Nickel-Ferrite and Cerium-Oxide Redox Materials for Two-Step Thermochemical Water Splitting Below 1400 °C," Proceedings of the ASME 2011 5th International Conference on Energy Sustainability, Washington, DC, Aug. 7–10.
[87] Otsuka, K., Kaburagi, T., Yamada, C., and Takenaka, S., 2003, "Chemical Storage of Hydrogen by Modified Iron Oxides," J. Power Source., **122**, pp. 111–21.
[88] Farmer, J. T., and Howell, J. R., 1998, "Comparison of Monte Carlo Strategies for Radiative Transfer in Participating Media," *Advances in Heat Transfer*, Vol. 31, J. P. Hartnett, T. F. Irvine, Jr., Y. I. Cho, and G. A. Greene, eds., Academic Press, New York, pp. 333–429.
[89] Chai, J. C., and Patankar, S. V., 2000, "Finite-Volume Method for Radiation Heat Transfer," *Advances in Numerical Heat Transfer*, Vol. 2, W. J. Minkowycz, and E. M. Sparrow, eds., Taylor & Francis, New York, pp. 109–141.
[90] Martinek, J., and Weimer, A. W., 2013, "Evaluation of Finite Volume Solutions for Radiative Heat Transfer in a Closed Cavity Solar Receiver for High Temperature Solar Thermal Processes," Int. J. Heat Mass Tran., **58**, pp. 585–596.
[91] Piatkowski, N., Wieckert, C., Weimer, A. W., and Steinfeld, A., 2011, "Solar-Driven Gasification of Carbonaceous Feedstock—A Review," Energ. Environ. Sci., **4**, pp. 73–82.
[92] Z'Graggen, A., and Steinfeld, A., 2008, "A Two-Phase Reactor Model for the Steam-Gasification of Carbonaceous Materials Under Concentrated Thermal Radiation," Chem. Eng. Process., **47**, pp. 655–662.
[93] Z'Graggen, A., and Steinfeld, A., 2009, "Heat and Mass Transfer Analysis of a Suspension of Reacting Particles Subjected to Concentrated Solar Radiation—Application to the Steam-Gasification of Carbonaceous Materials," Int. J. Heat Mass Tran., **52**, pp. 385–395.
[94] Lipiński, W., and Steinfeld, A., 2005, "Transient Radiative Heat Transfer Within a Suspension of Coal Particles Undergoing Steam Gasification," Heat Mass Transfer, **41**, pp. 1021–1032.
[95] Lipiński, W., Z'Graggen, A., and Steinfeld, A., 2005, "Transient Radiation Heat Transfer Within a Nongray Nonisothermal Absorbing-Emitting-Scattering Suspension of Reacting Particles Undergoing Shrinkage," Numer. Heat Trans. B., **47**, pp. 443–457.
[96] von Zedtwitz, P., Lipiński, W., and Steinfeld, A., 2007, "Numerical and Experimental Study of Gas-Particle Radiative Heat Exchange in a Fluidized-Bed Reactor for Steam-Gasification of Coal," Chem. Eng. Sci., **62**, pp. 599–607.
[97] Melchior, T., Perkins, C., Weimer, A. W., and Steinfeld, A., 2008, "A Cavity-Receiver Containing a Tubular Absorber for High-Temperature Thermochemical Processing Using Concentrated Solar Energy," Int. J. Therm. Sci., **47**, pp. 1496–1503.

[98] Melchior, T., and Steinfeld, A., 2008, "Radiative Transfer Within a Cylindrical Cavity With Diffusely/Specularly Reflecting Inner Walls Containing an Array of Tubular Absorbers," ASME J. Sol. Energy Eng., **130**(2), p. 021013.
[99] Loutzenhiser, P., Meier, A., and Steinfeld, A., 2010, "Review of the Two-Step H_2O/CO_2-Splitting Solar Thermochemical Cycle Based on Zn/ZnO Redox Reactions," Materials, **3**, pp. 4922–4938.
[100] Perkins, C., and Weimer, A., 2008, "Computational Fluid Dynamics Simulation of a Tubular Aerosol Reactor for Solar Thermal ZnO Decomposition," ASME J. Sol. Energy Eng., **129**(4), pp. 391–404.
[101] Haussener, S., Hirsch, D., Perkins, C., Weimer, A., Lewandowski, A., and Steinfeld, A., 2009, "Modeling of a Multitube High-Temperature Solar Thermochemical Reactor for Hydrogen Production," ASME J. Sol. Energy Eng., **131**(2), p. 024503.
[102] Abanades, S., Charvin, P., Flamant, G., 2007, "Design and Simulation of a Solar Chemical Reactor for the Thermal Reduction of Metal Oxides: Case Study of Zinc Oxide Dissociation," Chem. Eng. Sci., **62**, pp. 6323–6333.
[103] Lipiński, W., Thommen, D., and Steinfeld, A., 2006, "Unsteady Radiative Heat Transfer Within a Suspension of ZnO Particles Undergoing Thermal Dissociation," Chem. Eng. Sci., **61**, pp. 7029–7035.
[104] Dombrovsky, L. A., Lipiński, W., and Steinfeld, A., 2007, "A Diffusion-Based Approximate Model for Radiation Heat Transfer in a Solar Thermochemical Reactor," J. Quant. Spetrosc. Ra., **103**, pp. 601–610.
[105] Müller, R., and Steinfeld, A., 2007, "Band-Approximated Radiative Heat Transfer Analysis of a Solar Chemical Reactor for the Thermal Dissociation of Zinc Oxide," Solar Energ., **81**, pp. 1285–1294.
[106] Müller, R., Lipiński, W., and Steinfeld, A., 2008, "Transient Heat Transfer in a Directly Irradiated Solar Chemical Reactor for the Thermal Dissociation of ZnO," Appl. Therm. Eng., **28**, pp. 524–531.
[107] Meier, A., and Sattler, C., 2009, "Solar Fuels From Concentrated Sunlight," SolarPACES Report.
[108] Trombe, F., and Vinh, A. L. P., 1973, "Thousand kW Solar Furnace, Built by the National Center of Scientific Research, in Odeillo (France)," Solar Energ., **15**, pp. 57–61.
[109] Hirsch, D., Von Zedtwitz, P., Osinga, T., Kinamore, J., and Steinfeld, A., 2003, "A New 75 kW High-Flux Solar Simulator for High-Temperature Thermal and Thermochemical Research," ASME J. Sol. Energy Eng., **125**(1), pp. 117–120.
[110] Petrasch, J., Coray, P., Meier, A., Brack, M., Häberling, P., Wuillemin, D., and Steinfeld, A., 2007, "A Novel 50 kW 11,000 Suns High-Flux Solar Simulator Based on an Array of Xenon Arc Lamps," ASME J. Sol. Energy Eng., **129**(4), pp. 405–411.
[111] Krueger, K. R., Davidson, J. H., and Lipiński, W., 2011, "Design of a New 45 kWe High-Flux Solar Simulator for High-Temperature Solar Thermal and Thermochemical Research," ASME J. Sol. Energy Eng., **133**(1), p. 011013.
[112] Krueger, K. R., Lipiński, W., and Davidson, J. H., "Operational Performance of the University of Minnesota 45 kWe High-Flux Solar Simulator," ASME J. Solar Energ. Eng. (in press).
[113] Thalhammer, E., 1979, "Heliostat Beam Characterization System—-Update" Proceedings of the ISA/79 Conference, Chicago, IL, pp. 505–521.
[114] Strachan, J. W., 1992, "Revisiting the BCS, A Measurement System for Characterizing the Optics of Solar Collectors," Proceedings of the 39th International Symposium of Instrument Society of America.
[115] Kaluza, J., and Neumann, A., 2001, "Comparative Measurements of Different Solar Flux Gauge Types," ASME J. Sol. Energy Eng., **123**(3), pp. 251–255.
[116] Ballestrín, J., Ulmer, S., Morales, A., Barnes, A., Langley, L. W., and Rodríguez, M., 2003, "Systematic Error in the Measurement of Very High Solar Irradiance," Sol. Energ. Mat. Sol. Cell., **80**, pp. 375–381.
[117] Ballestrín, J., Rodríguez-Alonso, M., Rodriguez, J., Cañadas, I., Barbero, F., Langley, L. W., and Barnes, A., 2006, "Calibration of High-Heat-Flux Sensors in a Solar Furnace," Metrologia, **43**, pp. 495–500.
[118] Erickson, B., and Petrasch, J., 2012, "Inverse Identification of Intensity Distributions From Multiple Flux Maps in Concentrating Solar Applications," Eurotherm Conference No. 95: Computational Thermal Radiation in Participating Media IV, J. Phys. Conf. Ser., **369**, p. 012014.
[119] Z'Graggen, A., Friess, H., and Steinfeld, A., 2007, "Gas Temperature Measurement in Radiating Environments Using a Suction Thermocouple Apparatus," Meas. Sci. Tech., **18**(11), pp. 3329–3334.
[120] Lorenson, C., 1997, "Use of Imaging Pyrometry Sensor in Metallurgical Processes," *Sensors and Modeling in Materials Processing: Techniques and Applications*, Proceedings of a Symposium on the Application of Sensors and Modeling to Materials Processing, 126th Annual Meeting of the Minerals, Metals, and Materials Society, pp. 199–205.
[121] Tschudi, H. R., and Morian, G., 2001, "Pyrometric Temperature Measurements in Solar Furnaces," ASME J. Sol. Energy Eng., **123**(2), pp. 164–170.
[122] Kerr, C., and Ivey, P., 2004, "Optical Pyrometry for Gas Turbine Aeroengines," Sensor Rev., **24**, pp. 378–86.
[123] Rohner, N., and Neumann, A., 2003, "Measurement of High Temperatures in the DLR Solar Furnace by UV-B Detection," ASME J. Sol. Energy Eng., **125**(2), pp. 152–158.
[124] Hernandez, D., Olalde, G., Gineste, J. M., and Gueymard, C., 2004, "Analysis and Experimental Results of Solar-Blind Temperature Measurements in Solar Furnaces," ASME J. Sol. Energy Eng., **126**(1), pp. 645–653.
[125] Freid, A. P., Johnson, P. K., Musella, M., Müller, R., Steinbrenner, J. E., and Palumbo, R. D., 2005, "Solar Blind Pyrometer Temperature Measurements in High Temperature Solar Thermal Reactors: A Method for Correcting the System-Sensor Cavity Reflection Error," ASME J. Sol. Energy Eng., **127**(1), pp. 86–93.
[126] Pfänder, M., Lupfert, E., and Heller, P., 2006, "Pyrometric Temperature Measurements on Solar Thermal High Temperature Receivers," ASME J. Sol. Energy Eng., **128**(3), pp. 285–292.
[127] Pfänder, M., Hernandez, D., Neumann, A., Lüpfert, E., Lipiński, W., Tschudi, H.-R., and Ballestrín, J., 2006, "Solar-Blind Pyrometric Temperature Measurements Under Concentrated Solar Radiation," V. Ruiz, D. Martínez, M. Silva, M. Romero, and M. Brown, eds., Proceedings of the 13th SolarPACES International Symposium on Concentrating Solar Power and Chemical Energy Technologies, Seville, June 20–23.
[128] Smurov, I., Doubenskaia, M., and Bertrand, P., 2006, "Pyrometry in Laser Surface Treatment," Surf. Coat. Tech., **201**, pp. 1955–1961.
[129] Muller, M., Fabbro, R., El-Rabii, H., and Hirano, K., 2012, "Temperature Measurement of Laser Heated Metals in Highly Oxidizing Environment Using 2D Single-Band and Spectral Pyrometry," J. Laser Appl., **24**, p. 022006.
[130] Tschudi, H. R., and Schubnell, M., 1995, "Simultaneous Measurement of Irradiation, Temperature and Reflectivity on Hot Irradiated Surfaces," Appl. Phys. A., **60**, pp. 581–587.
[131] Schubnell, M., Tschudi, H. R., and Müller, C., 1996, "Temperature Measurement Under Concentrated Radiation," Solar Energ., **58**, pp. 69–75.
[132] Tschudi, H. R., and Schubnell, M., 1999, "Measuring Temperatures in the Presence of External Radiation by Flash Assisted Multiwavelength Pyrometry," Rev. Sci. Instrum., **70**, pp. 2719–2727.
[133] Hernandez, D., Ciaurriz, C., and Olalde, G., 1991, "Détermination de l'émissivité à haute température à l'aide de systèmes à fibres optiques équipés d'hémisphères réflecteures," J. Phys. III, **1**, pp. 1575–1586.
[134] Hernandez, D., Olalde, G., Beck, A., and Milcent, E., 1995, "Bicolor Pyroreflectometer Using an Optical Fiber Probe," Rev. Sci. Instrum., **66**, pp. 5548–5551.
[135] Hernandez, D., and Milcent, E., 1995, "Pyro-réflectomètre bicolore à fibres optiques pour mesures in situ," J. Phys. III, **5**, pp. 999–1011.
[136] Crane, N. B., 2010, "Pyrometric Temperature Measurement in Concentrated Sunlight With Emissivity Determination," ASME J. Sol. Energy Eng., **132**(1), p. 011007.
[137] Alxneit, I., 2011, "Measuring Temperatures in a High Concentration Solar Simulator—Demonstration of the Principle," Solar Energ., **85**, pp. 516–522.
[138] Guesdon, C., Alxneit, I., Tschudi, H. R., Wuillemin, D., and Sturzenneger, M., 2006, "1 kW Imaging Furnace With *In Situ* Measurement of Surface Temperature," Rev. Sci. Instrum., **77**, p. 035102.